

JGR Solid Earth

RESEARCH ARTICLE

10.1029/2021JB022106

Key Points:

- Systematic phase-field study captures formation of a wide range of single seal veins in limestones and provides insight to fracture healing
- Effects of different parameters are illustrated in morphology maps and show diagnostic microstructures
- Transgranular fracturing leads to stretched crystals and intergranular fracturing leads to more prominent CPO in syntaxial veins

Supporting Information:

Supporting Information may be found in the online version of this article.

Correspondence to:

M. Späth,
michael.spaeth@kit.edu

Citation:

Späth, M., Spruženiece, L., Urai, J. L., Selzer, M., Arndt, M., & Nestler, B. (2021). Kinematics of crystal growth in single-seal syntaxial veins in limestone - A phase-field study. *Journal of Geophysical Research: Solid Earth*, 126, e2021JB022106. <https://doi.org/10.1029/2021JB022106>

Received 23 MAR 2021
Accepted 1 SEP 2021

© 2021. The Authors.

This is an open access article under the terms of the [Creative Commons Attribution License](#), which permits use, distribution and reproduction in any medium, provided the original work is properly cited.

Kinematics of Crystal Growth in Single-Seal Syntaxial Veins in Limestone - A Phase-Field Study

Michael Späth¹ , Liene Spruženiece² , Janos L. Urai² , Michael Selzer^{1,3} , Max Arndt², and Britta Nestler^{1,3}

¹Institute for Applied Materials (IAM-CMS), Karlsruhe Institute of Technology (KIT), Karlsruhe, Germany, ²Institute of Tectonics and Geodynamics, RWTH Aachen University, Aachen, Germany, ³Institute of Digital Materials Science (IDM), Karlsruhe University of Applied Sciences, Karlsruhe, Germany

Abstract Building on recent developments in phase-field modeling of structural diagenesis, we present an analysis of single-seal syntaxial calcite vein microstructure in a variety of limestones. We focus on the effects of fracture aperture, intergranular versus transgranular fracturing, crystal habit and the presence of second phases in the host rock, to systematically investigate a simplified set of models covering the main classes of limestone in 2D. We incorporate the kinematic process of growth competition between differently oriented crystals, growth rate anisotropy between rough and faceted crystal surfaces and different growth rates on intergranular to transgranular fractures. Results show that within the considered parameter space we can reproduce a wide range of vein microstructures in limestone known in nature, such as stretched crystals, wide-blocky veins, and elongated crystals. We identify five archetypes of vein microstructures in limestones, which are diagnostic for different kinematics and evolution of transport processes and illustrate the effect of key parameters in microstructure maps. We show how syntaxial veins with median line form after intergranular fracturing, while stretched crystals indicate transgranular fracturing. Intergranular fracturing leads to stronger growth competition and more prominent CPO in syntaxial veins. Our results can be extended to 3D to include multiple crack-seal events, pore-space cementation and simulation of fluid flow, providing a generic platform for modeling structural diagenesis in limestones.

Plain Language Summary Fractures are ubiquitous in the earth crust, forming important pathways for geothermal fluids. This fluid is often supersaturated, allowing crystals to grow in the open fractures which leads to fracture healing over time. During this self-sealing of the fractured rock the permeability and strength of the rock change with many important consequences for subsurface engineering. In this study, we simulate the complex growth process and show how different crystal structures (e.g., stretched, blocky) form in open fractures in different types of limestone and compare our results to natural rock samples. We test different factors on how they affect the crystal morphology as fracture type (crack cuts through grain or along grain boundaries), opening width of the fracture, and coated grain surfaces (which can reduce the crystal growth rate). We are able to reproduce a wide range of crystal structures which occur in natural limestone, and present a framework for interpreting the evolution process of calcite veins in limestones. The systematic data analysis provides valuable insight in structure-property linkages enabling a prediction of fracture healing mechanisms.

1. Introduction

The chemistry and mechanics of fracture sealing in deforming hydrothermal and reactive environments is important in basic geoscience and applied studies. Examples are the seismic cycle (e.g., Alexandrakos et al., 2014), evolution of ore deposits (e.g., Cox et al., 1987; Sibson et al., 1988), geothermal energy (e.g., McNamara et al., 2016), and the production and injection of fluids from and into the subsurface (e.g., Almansour et al., 2020).

In dilatant fractures, aqueous fluids can dissolve or precipitate minerals, and this in turn affects the transport and mechanical properties of the rock system. Syntectonic syntaxial calcite or quartz veins are ubiquitous in rocks at low metamorphic grades in the upper and middle crust (Passchier & Trouw, 2005; Ramsay & Huber, 1983). The formation of these veins includes multiple coupled mechanical, hydraulic,

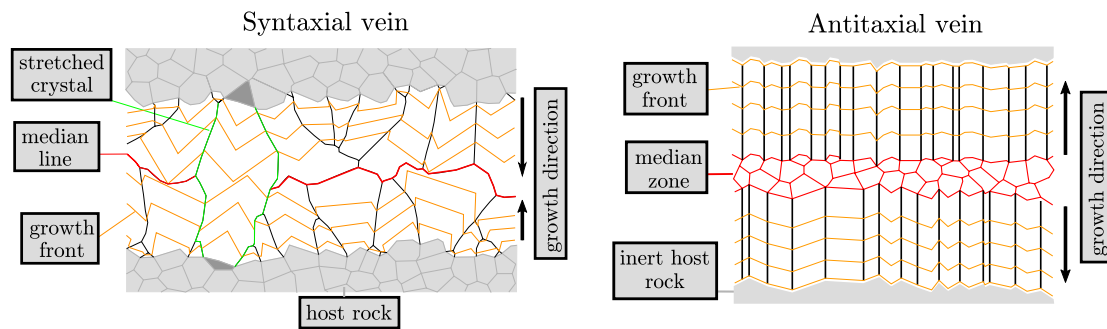


Figure 1. Schematic representation of a syntaxial vein on left and an antitaxial vein on right. Initial host rock is highlighted in gray, intermediate growth stages (growth front) in orange, and median line (in syntaxial veins) and median zone (in antitaxial veins) in red. The growth direction (arrows) is in syntaxial veins from the host rock inwards to the vein center and in antitaxial veins from the median zone (substrate) outwards to the host rock.

and geochemical processes and parameters (e.g., temperature, chemical composition, pressure of fluid) and results in a broad spectrum of macro- and microstructures (Laubach et al., 2019). Veins can be used to reconstruct the history of stress and fluid pressure (Bons et al., 2012). Chemical and isotope analysis of vein cement (Arndt et al., 2014) and fluid inclusions provide evidence on the thermal and chemical environment during vein formation and can be used to draw conclusions on fluid flow and mass transfer in the system (Boullier & Robert, 1992; Cox, 2007; Fisher & Brantley, 1992). However, the evolution of vein microstructures (Durney, 1973; Passchier & Trouw, 2005; Ramsay & Huber, 1983) remains an open field (e.g., influence of fracture type).

Urai et al. (1991) presented the first model to explain the kinematics of crystal growth into irregular spaces and the evolution from euhedral into nonSchmidegg shapes (Schmidegg, 1928). This work was extended by Nollet et al. (2005), who explored the transition from crystallographically rough surfaces to faceted crystals and back to irregular shapes, when crystals grow against a rough wall-rock surface. Depending on growth direction (syntaxial, antitaxial, bitaxial, unitaxial Durney, 1973), fracture location (localized, delocalized), opening trajectory of the fracture, fracture type (intergranular, transgranular), and mineral type (e.g., calcite, quartz) a broad variety of vein morphologies with different characteristic microstructures can form (e.g., fibrous, elongated-blocky, stretched, ataxial crystals) (Bons et al., 2012). Becker et al. (2011) demonstrated how the presence of a second mineral affects the crystal morphology in syntaxial bi-mineralic multi crack-seal veins.

In syntaxial veins crystals grow from both sides of the fracture wall inwards into the center, whereas in antitaxial veins crystals grow epitaxially on one side of the fracture from a median zone in the vein center outwards toward the inert wall rock surface (Durney, 1973) (Figure 1). Since antitaxial veins have a different mineralogy than the wall rock (lower adhesion), the fracture opens at the vein-host rock interface and the opening and sealing occur continuously (e.g., due to force of crystallization) or in a sequential pattern. When opening increments are small, the development of crystal facets is limited and fibrous crystals can form (Ankit et al., 2013; Ankit, Selzer, et al., 2015; Bons et al., 2012; Hilgers et al., 2001; Nollet et al., 2005; Urai et al., 1991). The numerical modeling of antitaxial veins has two big advantages: (1) the sealed crack is very weak and will reopen in the same location so that the fracture mechanics is simple, and (2) crystals grow against an inert wall, so that the joining of crystals growing from both sides does not have to be simulated. Urai et al. (1991) developed a kinematic model for the formation of these veins and investigated the effect of the fracture wall roughness on the evolving microstructure. Expanding on this work, sharp interface methods, which explicitly track the growth front, have been utilized in 2D to understand the influence of opening velocity and trajectory in antitaxial veins (e.g., Vein Growth (Bons, 2001; Hilgers et al., 2001) or FACET (Zhang & Adams, 2002)).

The vast majority of veins in limestone consist of calcite which grows epitaxially on the calcite grains in the host rock. They are called syntaxial or ataxial veins due to the crystal growth from both sides toward the fracture interior (Hilgers et al., 2001; Passchier & Trouw, 2005). For simulations, this has two additional problems: (1) the sealed crack is strong and can reopen at a different location so that mechanics of

fracturing is complicated and can be delocalized, and (2) crystals grow from opposite sides of the crack, so that simulations have to be performed against dynamic interfaces, instead of inert fracture walls.

The cellular-automaton-type program Prism2D (Lander et al., 2008) has been applied for crystal growth in syntaxial veins (in quartz: Lander et al., 2008; Lander & Laubach, 2015, in dolostone: Gale et al., 2010). In their numerical model they incorporated the well-known effect that crystals, which grow on rough surfaces, show a significant decrease in the total growth velocity after they attain their faceted shapes (see e.g., Periodic Bond Chain theory from Hartman & Perdok, 1955a, 1955b, 1955c). Their numerical model has been calibrated with quartz growth kinetics from laboratory experiments (Lander et al., 2008).

The phase-field method is widely used in material science for modeling microstructure evolution processes. This method uses a mathematical model to represent an interface, in this case for growing crystals (Fix, 1982; Langer, 1980, 1986). It is based on the local energy functional minimization and allows with its diffuse interface approach an elegant treatment of moving boundary problems where no explicit interface-tracking algorithm is required. Recently, the phase-field method has emerged as a powerful tool to model cementation of fracture and matrix porosity in the subsurface (see e.g., Ankit, Urai, & Nestler, 2015; Hubert et al., 2009; Wendler et al., 2016). It allows the investigation of different vein mineralogies, such as potash alum (Ankit et al., 2013), quartz (Ankit, Urai, & Nestler, 2015; Prajapati, Abad Gonzalez, et al., 2020; Wendler et al., 2016) or calcite (Prajapati et al., 2018; Spruženiece et al., 2020, 2021) in 2D and 3D.

In one of the first phase-field studies of antitaxial vein formation Hubert et al. (2009) utilized a nonfaceted smooth anisotropy formulation in the interfacial energy term for the modeling of antitaxial vein growth, whereas in nature crystals are flat faceted crystals with sharp corners. This limitation was overcome by the work of Ankit et al. (2013), who utilized a facet-type anisotropy formulation in the interfacial energy term (see e.g., Nestler et al., 2005). In this and a subsequent work (Ankit et al., 2013; Ankit, Selzer, et al., 2015) studies of antitaxial vein formation were conducted in 2D and 3D with varying fracture roughness, opening velocity, increment and trajectory, and showed a sound agreement with previous works of Urai et al. (1991) and Hilgers et al. (2001). However, antitaxial veins are relatively rare in limestones. They typically form in shales, marls and silty mudstones and consist of calcite, gypsum and halite (e.g., Cobbold et al., 2013; Hilgers & Urai, 2002; Leitner et al., 2014; Meng et al., 2019; Philipp, 2008).

The same phase-field model as in Ankit et al. (2013) has been applied in Ankit, Urai, and Nestler (2015) for studying in 3D multi-crack-seal events in syntaxial quartz veins with normal and oblique openings, and in Prajapati et al. (2018) for modeling calcite vein formation. Therein, the evolution of different crystal morphologies with varying fracture opening velocities is demonstrated. In Wendler et al. (2016) the phase-field model parameters were calibrated to laboratory quartz growth experiments (e.g., Okamoto et al., 2010) by using anisotropy formulations in the interfacial energy term and the kinetic mobility. In order to incorporate the effect of different growth velocities for rough and faceted crystals the kinetic mobility parameter in the phase-field evolution equation was adapted. Additionally, they utilize an interpolation of the mobility in solid-liquid multiphase regions to avoid artifacts by triple point pinning. However, this approach is limited to grain structures, where all crystals have similar total growth velocities.

Recent studies of syntaxial calcite veins in limestones by Spruženiece et al. (2020, 2021) showed that in some veins the crystal growth rates vary depending on how the host rock grains are fractured (intergranular or transgranular). They utilized the anisotropy formulation of the kinetic mobility of Wendler et al. (2016) and combined it with the evolution equation of Steinbach (2009) to distinguish between fast-growing calcite crystals on transgranular fracture surfaces and slow-growing calcite crystals on intergranular fractures.

Limestones can have different mineral compositions and a wide spectrum in grain size distribution and crystal morphology. The grain- and crystal size distribution can vary from mm range (e.g., in crystalline limestone) to a few μm in e.g., mudstone (Dunham, 1962). Depending on the distribution of skeletal fragments (e.g., foraminifera, coral) the grain size differs from approximately equally sized grain structures (e.g., micrite, ooids) to mixed-sized structures, in which both fine and coarse grains occur (e.g., a fine-grained mud-dominated, nongrain supported limestone with at least 10% skeletal components, thus a wackestone). Figure 2 illustrates a diversity of veins in different limestone host rocks: mudstone, wackestone, and crystalline limestone. The vein microstructures vary from homogeneously sized crystals (stretched or bitaxial) over wide blocky crystals to elongated bladed crystals, depending on the host rock type and vein apertures.

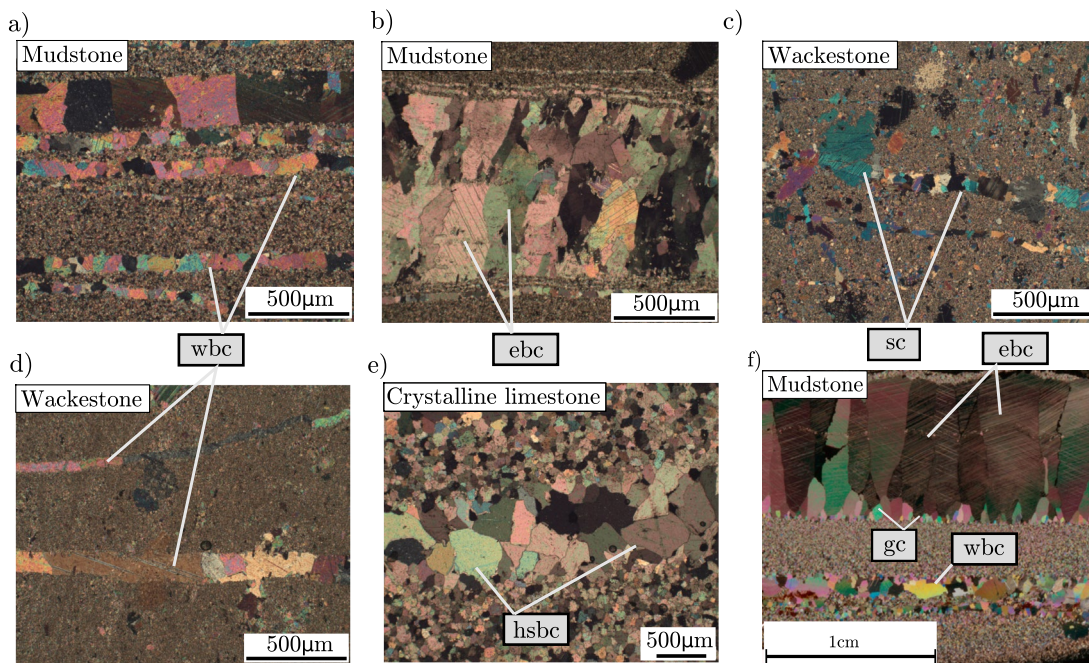


Figure 2. Photomicrographs of veins in different types of limestones (images are taken with transmitted light optical microscope under crossed polarizers and include calcite crystals): (a and b) Mudstone from Lilstock beach, UK; (c and d) Wackestone from Oman Mountains; (e) Crystalline limestone from Oman Mountains. (f) Veins with different apertures in mudstone from Oman Mountains showing different vein microstructures (adapted from Figure B1 in Arndt, 2016). wbc: wide-blocky crystal; hsbc: homogeneously sized blocky crystal; ebc: elongated bladed crystal; sc: stretched crystal; gc: growth competition.

In addition, depending on the host rock composition and fracturing conditions, the fracture surface can be highly heterogeneous, exposing varying amounts of intergranular and transgranular segments (Figure 3), as well as surfaces of accessory minerals, which are unfavorable for the nucleation and growth of vein crystals (Aubert et al., 2020; Spruženiece et al., 2020).

Even though previous studies examined how the fracture surface characteristics affect crystal growth in veins (Ajdukiewicz & Larese, 2012; Lander & Laubach, 2015; Lander et al., 2008; Urai et al., 1991; Williams et al., 2015), they mostly focused either on the fracture geometry or growth kinetics of single crystals.

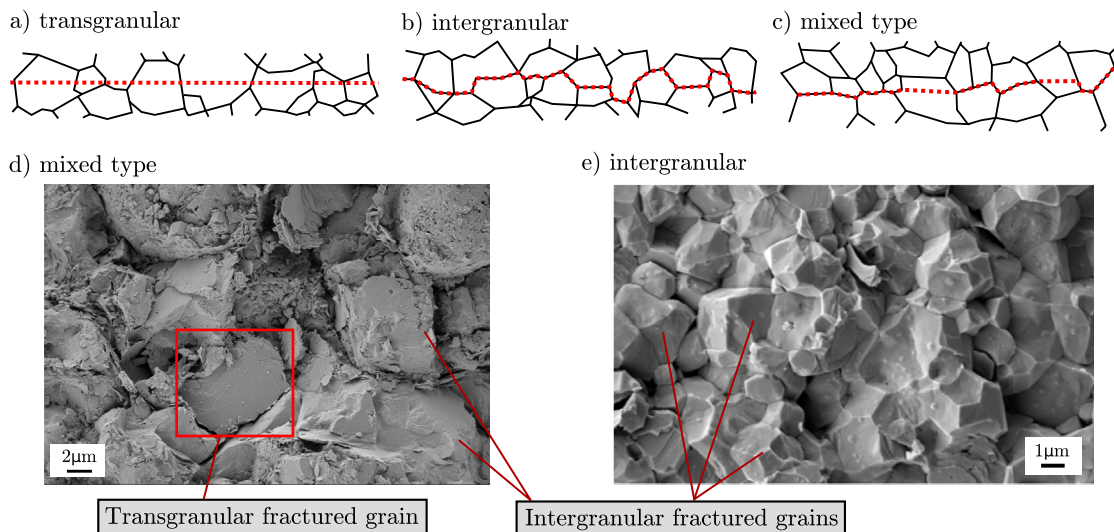


Figure 3. (a–c) Considered fracturing types in this study. (d and e) Secondary electron images of experimentally fractured mudstone host rock. Red box indicates transgranular fractured grain. (e) Adapted from Figure 3.21 in Arndt (2016).

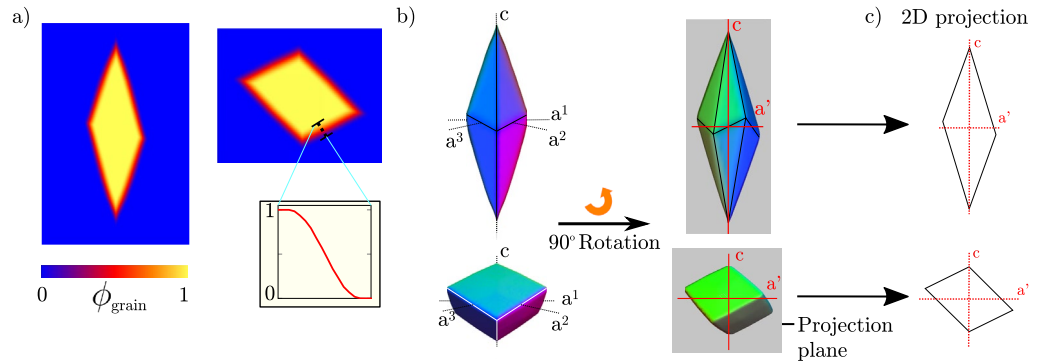


Figure 4. Representative crystal habits in calcite used in the simulated veins: (a) The phase-field order parameter increases continuously from 0 to 1 within the diffuse interface region (reddish). (b) Scalenohedral (top) and rhombohedral (bottom) shape in 3D with crystallographic axis. (c) Right handed projections of scalenohedral and rhombohedral shape in 2D simulations.

In this work, we build on these previous works aiming to provide a systematic framework for understanding the diversity of vein microstructures in limestone host rocks (Figure 2) and generalize the occurring morphologies. We incorporate diverse limestone host rock microstructures and complex fracture cements in our models, similar to those that occur in natural limestones. We focus on the formation of syntaxial calcite veins in limestone and investigate single crack-seal events, where, after the initial opening and sealing, no repeated fracturing occurs.

2. Methods

2.1. Multiphase-Field Model

A thermodynamically consistent multiphase-field model (Nestler et al., 2005) is utilized to computationally investigate, characterize and classify crystal growth in limestone veins. The presented model was applied in the previous works of Spruženiece et al. (2020, 2021) and is briefly described in this section. For further discussions on the model equations interested readers are referred to for example Ankit, Urai, and Nestler (2015); Wendler et al. (2016); Prajapati, Abad Gonzalez, et al. (2020).

The phase-field model is based on local minimization of the Helmholtz free energy, which is given by

$$\mathcal{F}(\phi, \nabla \phi) = \int_{\Omega} \left[\varepsilon a(\phi, \nabla \phi) + \frac{1}{\varepsilon} w(\phi) + f_{\text{bulk}}(\phi) \right] d\Omega = \mathcal{F}_{\text{intf}} + \mathcal{F}_{\text{bulk}}, \quad (1)$$

where the N scalar phase-field order parameters $\phi_{\alpha}(x, t)$ are collectively represented by the phase-field vector $\phi(x, t) = [\phi_1(x, t), \dots, \phi_N(x, t)]$. Note: Bold symbols refer to vector quantities, whereas nonbold symbols indicate a scalar quantity. Each phase-field parameter $\phi_{\alpha}(x, t) \in [0, 1]$ indicates the presence of a liquid or solid phase and accordingly of an orientational crystallographic variant at position x and time t . In contrast to sharp interface models, a diffuse transition region of finite width characterizes the interface between different phases, where the length scale parameter ε controls the diffuse interface width. In diffuse interface regions, the magnitude of a phase-field ϕ_{α} continuously decreases from 1 inside the bulk phase to 0 outside (Figure 4a) and the summation constraint $\sum_{\alpha=1}^N \phi_{\alpha} = 1$ is ensured at each computational grid point.

In Equation 1, the interfacial energy density contribution is represented by the gradient energy density $\varepsilon a(\phi, \nabla \phi)$ and the potential free energy density $\frac{1}{\varepsilon} w(\phi)$, whereas $f_{\text{bulk}}(\phi)$ denotes the bulk free energy density, and $\nabla \phi$ is the gradient of the phase-field vector ϕ . The multi-obstacle potential energy density is given by

$$\frac{1}{\varepsilon} w(\phi) = \begin{cases} \frac{16}{\varepsilon \pi^2} \sum_{\alpha < \beta}^N \gamma_{\alpha\beta} \phi_{\alpha} \phi_{\beta} + \sum_{\alpha < \beta < \delta}^N \gamma_{\alpha\beta\delta} \phi_{\alpha} \phi_{\beta} \phi_{\delta} & \text{if } \phi \in \mathcal{G} \\ \infty & \text{else,} \end{cases} \quad (2)$$

where $\mathcal{G} = \{\phi | \sum_{\alpha} \phi_{\alpha} = 1, \text{ and } \phi_{\alpha} \geq 0\}$ is the Gibbs simplex. The occurrence of unphysical higher order phases in binary interfaces is reduced by the second sum. The gradient energy density is denoted as

$$\varepsilon a(\phi, \nabla(\phi)) = \varepsilon \sum_{\alpha < \beta}^N \gamma_{\alpha\beta} a_{\alpha\beta}^2(\phi, \nabla\phi) |\mathbf{q}_{\alpha\beta}|^2, \quad (3)$$

with the interface normal vector $\mathbf{q}_{\alpha\beta} = \phi_{\alpha} \nabla \phi_{\beta} - \phi_{\beta} \nabla \phi_{\alpha}$ and the surface energy density $\gamma_{\alpha\beta}$ of an α - β interface. The gradient energy density function can be modeled anisotropic by adapting the factor $a_{\alpha\beta}$, where the choice of $a_{\alpha\beta} = 1$ leads to an isotropic shape. A faceted crystal growth is modeled with a piecewise defined anisotropic surface energy function

$$a_{\alpha\beta}(\phi, \nabla\phi) = \max_{1 \leq k \leq n_{\alpha\beta}} \{\hat{\mathbf{n}} \cdot \boldsymbol{\eta}_{k,\alpha\beta}\}, \quad (4)$$

where the unit normal vector is given by $\hat{\mathbf{n}} = \frac{\mathbf{q}_{\alpha\beta}}{|\mathbf{q}_{\alpha\beta}|}$ and $\{\boldsymbol{\eta}_{k,\alpha\beta} | k = 1, \dots, n_{\alpha\beta}\}$ are the $n_{\alpha\beta}$ corners of the Wulff shape.

Moreover, the bulk free energy density $f_{\text{bulk}}(\phi)$ is linearly interpolated in diffuse interface regions $f_{\text{bulk}}(\phi) = \sum_{\alpha} \phi^{\alpha} f_{\text{bulk}}^{\alpha}$.

The temporal evolution of each phase-field ϕ_{α} is described with the variational derivative of the energy functional (Equation 1). We adopt the approach of Steinbach (2009) to apply different mobilities (growth velocities) for different phases without interpolation difficulties of the kinetic mobility in multi-phase regions. The evolution equation reads as

$$\frac{\partial \phi_{\alpha}}{\partial t} = -\frac{1}{N\varepsilon} \sum_{\alpha \neq \beta}^N \left[M_{\alpha\beta}(\hat{\mathbf{n}}) \left(\frac{\delta \mathcal{F}_{\text{intf}}}{\delta \phi_{\alpha}} - \frac{\delta \mathcal{F}_{\text{intf}}}{\delta \phi_{\beta}} - \frac{8\sqrt{\phi_{\alpha}\phi_{\beta}}}{\pi} \left(\frac{\delta \mathcal{F}_{\text{bulk}}}{\delta \phi_{\beta}} - \frac{\delta \mathcal{F}_{\text{bulk}}}{\delta \phi_{\alpha}} \right) \right) \right] \quad (5)$$

where the mobility coefficient $M_{\alpha\beta}(\hat{\mathbf{n}})$ of the α - β interface is denoted by

$$M_{\alpha\beta}(\hat{\mathbf{n}}) = M_{\alpha\beta}^0 a_{\alpha\beta}^{\text{kin}}(\hat{\mathbf{n}}), \quad (6)$$

with the kinetic coefficient $M_{\alpha\beta}^0$ and the kinetic anisotropy $a_{\alpha\beta}^{\text{kin}}(\hat{\mathbf{n}})$. For modeling a faster growth rate of rough crystal surfaces and a drop of the growth velocity after crystal facets have formed (Lander et al., 2008) we follow the approach of Wendler et al. (2016) and utilize

$$a_{\alpha\beta}^{\text{kin}}(\hat{\mathbf{n}}) = \left(1 + \delta \left(\max_k \{\hat{\mathbf{n}} \cdot \boldsymbol{\eta}_{k,\alpha\beta}\} - \max_{k-1} \{\hat{\mathbf{n}} \cdot \boldsymbol{\eta}_{k,\alpha\beta}\} \right) \right) \max_k \{\hat{\mathbf{n}} \cdot \boldsymbol{\eta}_{k,\alpha\beta}\} \quad (7)$$

for the kinetic anisotropy. The terms $\max_k \{\dots\}$ and $\max_{k-1} \{\dots\}$ denote the largest and the second largest argument of the scalar products. When the crystal is in its equilibrium shape, $\max_k \{\dots\}$ and $\max_{k-1} \{\dots\}$ are equal and the second argument (after δ) vanishes, whereas when the crystal is in a nonequilibrium/rough shape the largest and second largest argument differ. The drop of the growth rate between rough to fully faceted can be calibrated to experimental data with the factor δ (see e.g., Prajapati, Abad Gonzalez, et al., 2020; Wendler et al., 2016 for quartz).

2.2. Computational Treatment With Assumptions

The model equations are implemented in the in-house software package Pace3D (Parallel Algorithms for Crystal Evolution in 3D), which is written in language C. Interested readers are referred to Hötzer et al. (2018) for a detailed description of implemented optimization and parallelization algorithms.

The model parameters used in the simulations are given in Table 1. We choose the simulation parameters in order to ensure a numerically stable simulation, while reducing computational costs. When additional physical properties (e.g., chemical composition, pressure, temperature of the fluid) are available the non-dimensional simulation parameters could be mapped to physical values and information about the growth kinetics could be obtained (see e.g., Prajapati, Abad Gonzalez, et al., 2020; Wendler et al., 2016).

We assume, that precipitation is the rate-limiting step for the crystal growth, i.e., the attachment kinetics of the solute are slow compared to transport rate. This results in a constant supersaturation in the whole domain. Therefore, we utilize a constant chemical driving force f_{bulk}^{α} in the present work.

Table 1
Values of Phase-Field Model Parameters Used in Simulations

Model parameter	Value
Grid spacing Δx	1.0
Time-step Δt	0.035 (rhomb.) / 0.0035 (scal.)
Length scale parameter ε	6.5
Interfacial energy density $\gamma_{\alpha\beta}$	1.0
Higher order parameter $\gamma_{\alpha\beta\delta}$	20.0
Mobility of transgranular fractured grains to liquid $M_{\text{TFG,-liq}}^0$	1.0
Mobility of intergranular fractured grains to liquid $M_{\text{IFG,-liq}}^0$	0.0–1.0
Mobility of inert grains (e.g., silica) to liquid $M_{\text{inert,liq}}^0$	0.0
δ	1.0
Bulk energy density for crystals f_{bulk}^α	−0.25 (2D) / −0.5 (3D)

2.3. Modeling Crystal Shapes

The major minerals in limestone are calcite, dolomite, and aragonite, and these can have a wide range of crystal habits (Goldschmidt, 1913). In the present work we focus on calcite that is the most common component in limestone. Calcite can develop different crystal habits, depending on temperature, supersaturation and impurities in the solution, which can influence the vein microstructure (Gutjahr et al., 1996; Nollet et al., 2005; Paquette & Reeder, 1990; Plummer et al., 1979). For this study we choose rhombohedral and scalenohedral crystal habits, as they commonly appear in nature (Bishop et al., 1999; White & Culver, 2011). For the rhombohedral habit we apply the vectors in Equations 4 and 7 from Prajapati et al. (2017) with a c/a ratio of 0.86 (also given in Supporting Information S1), whereas we elongate the c -axis for the scalenohedral shape to obtain a c/a ratio of 3.41 in the 3D shape (e.g., Barber & Wenk, 1979; Gunasekaran et al., 2006; Sekkal & Zaoui, 2013). In Figure 4b the simulated 3D shapes for scalenohedral and rhombohedral calcite are depicted with the projections used in the 2D simulations (in a)). In the 2D projections the c/a' ratio is 1.02 and 3.32 for the rhombohedral and scalenohedral shape respectively (in Figure 4c).

2.4. Two Dimensional vs. Three Dimensional Models

Most of the simulations in the present work are performed in 2D to limit computational costs for setups with a large number of grains (from 890 to 14,660 grains). The 2D simulations are able to capture most aspects of the microstructure evolution, however the crystallographic orientation of the grains is only rotated perpendicular to the simulation plane and the third growth direction (out of plane) is not considered. Here we note that at higher computational cost, an extension to 3D in general is possible as presented in Section 3.6 in a representative setup.

2.5. Parameter Space and Boundary Conditions

In this study we investigate the influence of the following parameters on the grain structure in the veins: aperture, fracture type, grain size distribution, crystal habit, and mineralogical composition of the host rock. Table 2 illustrates the combinations of the parameters explored in the following subsections.

In order to easily compare the simulated veins to natural limestones, in which the host rock grain size can have different scales (crystalline limestone in mm range; mudstone in μm range (Dunham, 1962)), we scale the aperture of all simulated fractures by the average grain diameter in the host rock by expressing it as a dimensionless parameter D_m .

Table 2
Varied (x) and Constant (−) Parameters in Each Section in Results Chapter

	Sec. 3.1	Sec. 3.2	Sec. 3.3	Sec. 3.4	Sec. 3.5
Aperture	x	x	x	x	x
Fracture type	x	-	x	-	-
Grain size distribution	-	-	x	-	-
Accessory minerals	-	-	-	x	-
Crystal habit	-	-	-	-	x

The initial grain structures in the 2D and 3D computational domains were generated in a three-step process: (1) A host rock was generated with a Voronoi algorithm, in which the grain orientations are randomly distributed. Optionally, differently sized grain structures were combined to obtain the final host rock. (2) A fracture was inserted in the host rock, which cuts the grains either intergranularly or transgranularly. The fracture was created with a graphics editor and then converted into the data format of Pace3D. (3) The lower fracture wall was then shifted downwards in a direction perpendicular to the wall until the designated value for the opening aperture (e.g., $8D_m$). The opening of the fracture was performed in a single step and the crystal growth was initiated after the opening of the fracture, which corresponds to a faster opening than crystal growth rate. The phase-field models are set up such that the simulations stop, after the vein is completely sealed.

3. Results

3.1. Effect of the Fracture Surface Microstructure

In this section, we analyze different types of fracture surfaces that can occur in limestones, formed during intergranular, transgranular, and mixed type microcracking (Figure 3). We assume a growth rate difference between intergranular and transgranular fractured grains, which can result from clay coatings on intergranularly fractured grains, in which a fracture cuts through the clay and leaves a full or partial coating on the calcite grains. This remnant (partial) coating hinders the precipitation rate compared to freshly broken transgranular fractures. In contrast, a growth rate difference between different fracture types is not present, when, for example, a fracture cuts in between a grain and its coating or when the rock went through considerable primary pore space cementation and previous coatings are overgrown. We model the reduced growth rate on intergranular fracture surfaces as a decrease in the solid/liquid interface mobility $M_{\text{IFG-liq}}^0$, where the factor $\xi = M_{\text{TFG-liq}}^0 / M_{\text{IFG-liq}}^0$ describes the ratio between the solid/liquid mobility of transgranularly to intergranularly fractured grains (abbreviated with TFGs and IFGs in the next sections). A higher ξ corresponds to a larger growth rate difference, whereas $\xi = 1$ implies no growth rate difference. In the forthcoming sections we set $\xi = 5$ if not stated otherwise, which gives a sound agreement of the models to natural veins in micrite (Spruženiece et al., 2020).

In the next sections we refer to crystallographically controlled growth competition, when favorably oriented crystals outgrow and terminate unfavorably oriented crystals, whereas fracture-surface controlled growth competition occurs, when $\xi > 1$ and slow growing IFGs are terminated by faster growing TFGs.

The simulation setup ($160 \times 2500\Delta x$) for the investigation of the fracture type is depicted in Figure 5a. The percentage of intergranular fractured grains is varied from 0% to 100% and apertures of 2, 8, and $30D_m$ are examined. Furthermore, a computational fracture with an aperture of $300D_m$ with (1) 100% intergranular fracturing, and (2) mixed type fracturing ($\approx 87\%$ IFGs and 13% TFGs) is generated ($10000 \times 4600\Delta x$ with $\approx 6,300$ grains in Figure 7; Setup depicted in Supporting Information S1).

In the next sections we distinguish between the following crystal shapes: stretched-equidimensional (crystal height (h) approx. crystal width (w)), stretched-elongated ($h > w$), (stretched) wide-blocky ($w > h$), (bitaxial) blocky (h approx. w), and (bitaxial) elongated blocky ($w < h$). Stretched indicates that two fragments of a broken crystal from the opposite fracture wall join, whereas bitaxial indicates that different crystals reconnect in the vein center. Note: The term *stretched* is also used in multi-crack seal veins for crystals which are fractured and reconnect multiple times, whereas in this work only one sealing event occurs.

3.1.1. Pure Intergranular vs. Pure Transgranular Fractures

First we compare the crystal morphologies in a computational fracture with apertures of 2, 8, and $30D_m$, where either pure intergranular or pure transgranular fracturing occurs (Figures 5b and 5c). When all grains are fractured along the grain boundaries (100% intergranularly), the vein crystals grow euhedrally on the surfaces of the wall rock calcite grains and a distinct median line forms for all tested fracture apertures (highlighted with black line) and stretched crystals are absent. For small apertures ($2D_m$) a majority of crystals reach the vein center, where they terminate against differently oriented crystals from the opposite side of the fracture wall. When the aperture increases, more crystals are terminated at early stages of the vein

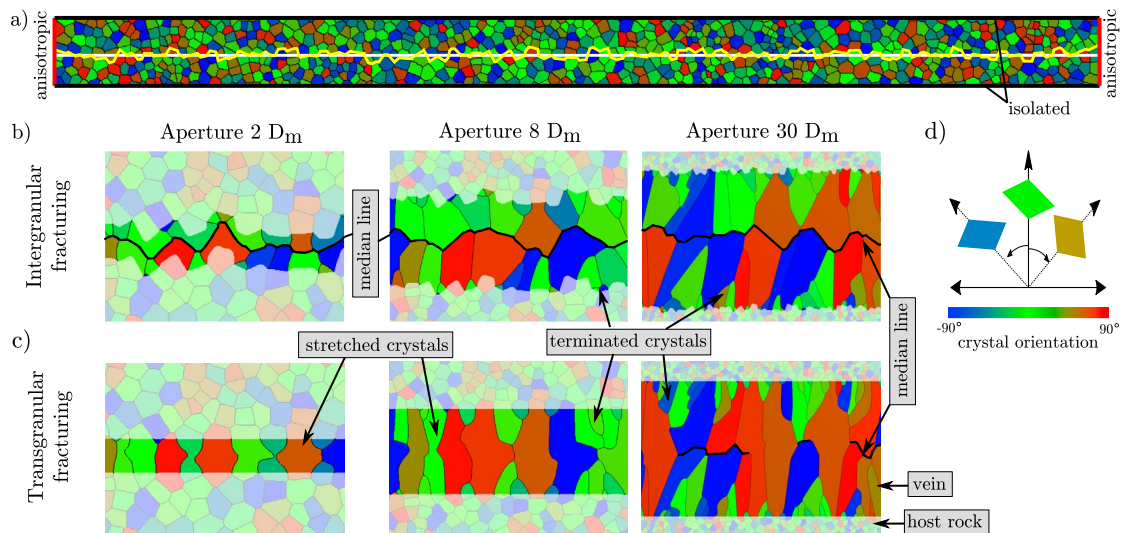


Figure 5. (a) Simulation setup with applied boundary conditions for pure intergranular (yellow line) and pure transgranular (white straight line) fracturing. (b) Fully sealed veins with apertures of 2, 8, and $30D_m$. Images show representative cut-outs from the final structures of pure (b) intergranular and (c) transgranular fractured host rock setups after sealing by calcite crystals (complete images in Supporting Information S1). The initial host rock structure is highlighted in white, the vein is in bright colors and the median line is indicated as black line. (d) Color bar indicates orientation of calcite c-axis with respect to the fracture opening direction in simulations with rhombohedral habit.

evolution as they are outcompeted by their favorably oriented neighbor crystals. In veins with the largest aperture, crystals with elongated and blade-like morphologies dominate but there is still a median line.

In the veins with pure TFGs, most crystals tend to bridge the vein in fractures with the smallest aperture ($2D_m$), as the transgranularly broken wall rock grains have the same crystallographic orientation on both sides of the fracture, resulting in stretched crystal morphologies. With an increased initial fracture aperture (e.g., $8D_m$) crystallographically controlled growth competition dominates and unfavorably oriented crystals are terminated. In some areas, when nonidentical crystal fragments meet in the vein center, a poorly defined median line is suggested. With a larger aperture more nonidentical fragments touch and the median line becomes more prominent. In the aperture of $30D_m$ still a few stretched crystals form and this structure shows similarities to the pure intergranular fractured veins.

3.1.2. Mixed Fracturing Type

In this section we analyze the simulations for mixed type fractures with varying ratios of intergranular and transgranular fracture segments. Based on previous studies (Spruzeniece et al., 2021) we assume different growth rates for the two types of fracture surfaces, which results in fracture surface-controlled growth competition. Representative cut-outs of the fully sealed veins are depicted in a morphology diagram in Figure 6a and the mean crystal size is plotted in Figure 6b. Therefore, the vertical simulation domain width (scaled by D_m) is divided by the number of crystals at the median line. The dominant crystal shapes in veins are classified in Figure 6c (see definitions in previous section). The complete images of the computational veins are given in the Supporting Information S1. Figure 6d shows the numbers of surviving crystals against the distance from the vein center (raw data given in repository). (Here, the fully sealed vein is equidistantly sliced and the number of occurring crystals in each slice is counted).

The porosity evolution in the veins of 2, 8, and $30D_m$ is plotted semi-logarithmically in Figure 6e. We normalize the porosity (or volume fraction of the liquid phase) for all apertures to the initial volume of liquid phase in the $30D_m$ vein. With a greater percentage of IFGs the duration of the sealing process increases, which results from the assignment of a reduced mobility of IFGs (due to their coated surfaces).

We observe a wide range of crystal morphologies, depending on the proportion of intergranular and transgranular segments on the initial fracture surfaces. Veins with stretched crystal morphologies, where TFGs tend to touch in the vein center, form in fractures with the smallest apertures if the intergranular fracture surfaces do not exceed 70%. Stretched-equidimensional crystals form in apertures of $2D_m$ and

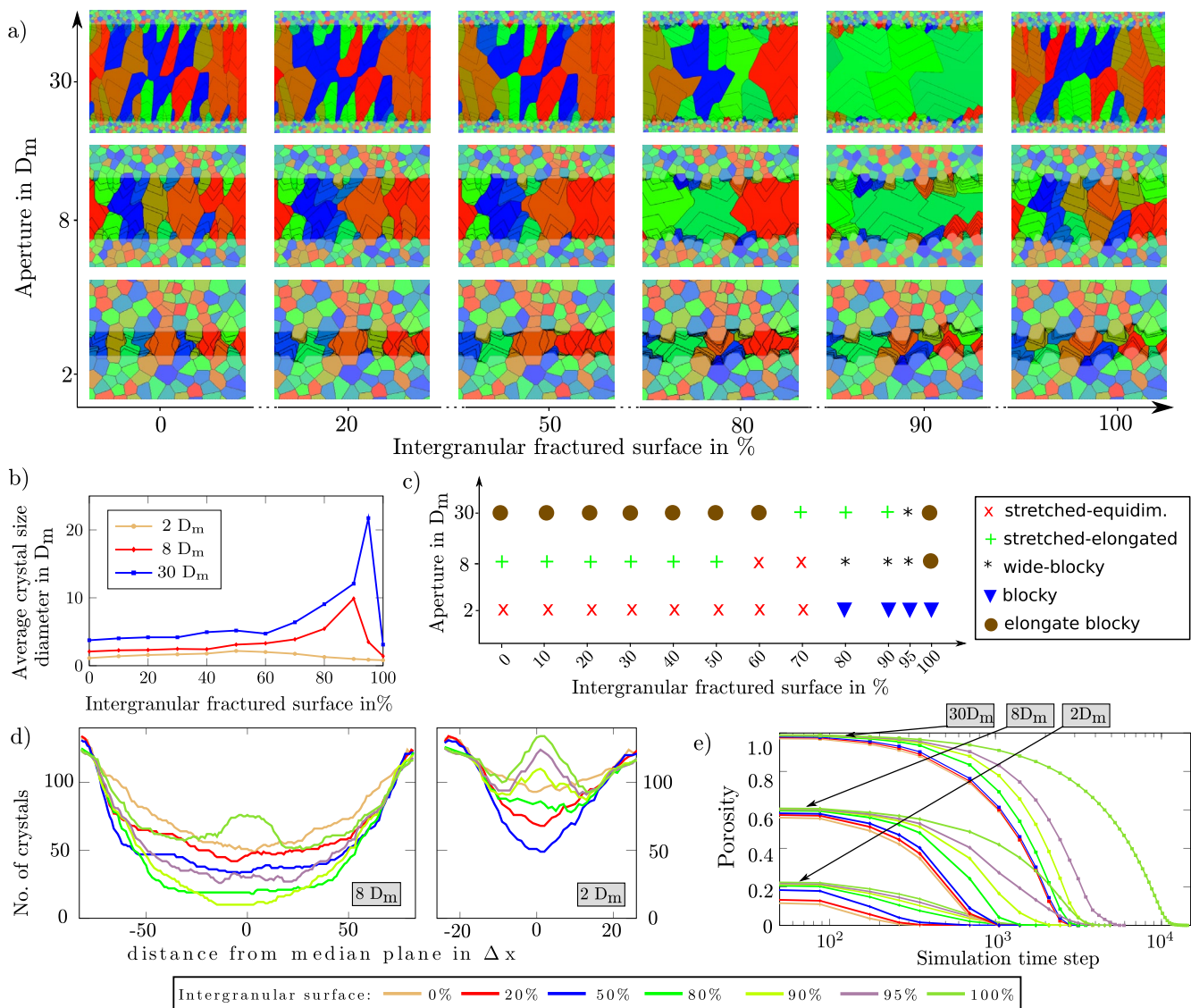


Figure 6. Simulations with different fracture surface types (with $\xi = 5$). (a) Morphology diagram showing vein microstructures at different initial fracture apertures and proportion of intergranularly fractured grains on the fracture. Images show representative cut-outs from the fully sealed veins (complete veins in Supporting Information S1). (b) Average crystal size (scaled by D_m) for 0%–100% intergranular fractured grains and (c) dominant crystal morphologies in the simulated veins. (d) Number of crystals with respect to the distance from the median plane in the vein ($30 D_m$ in Supporting Information S1). (e) Porosity loss during the fracture sealing (normalized by initial porosity of $30 D_m$ vein).

stretched-elongated crystals form in $8 D_m$ openings, whereas an increasing lateral expansion of the TFGs is observed with an increasing number of IFGs. In intermediate growth stages crystal bridges are observed, when TFGs have touched near the median line before they continue expanding laterally. Wide-blocky veins were only obtained in simulations with fracture apertures of $8 D_m$, where the proportion of intergranular fracture segments ranges from 80% to 95% and at the aperture $30 D_m$ with 95% IFGs. For the same range of IFGs in the $2 D_m$ veins blocky crystals occur, where the IFGs touch (median line visible), which block the TFGs from further lateral expansion. Elongated blocky crystals form mostly at the aperture of $30 D_m$, where crystallographically controlled growth competition between different TFGs and early termination of IFGs occurs. This leads to only few stretched-elongated crystals and more elongated blocky crystals.

In the veins with the aperture of $300 D_m$ (Figure 7) similar mechanisms occur. In the simulations on mixed fracturing type, IFGs are terminated at early stages and further crystallographically controlled growth competition proceeds exclusively between TFGs. The greater the distance between IFGs and TFGs is, the more

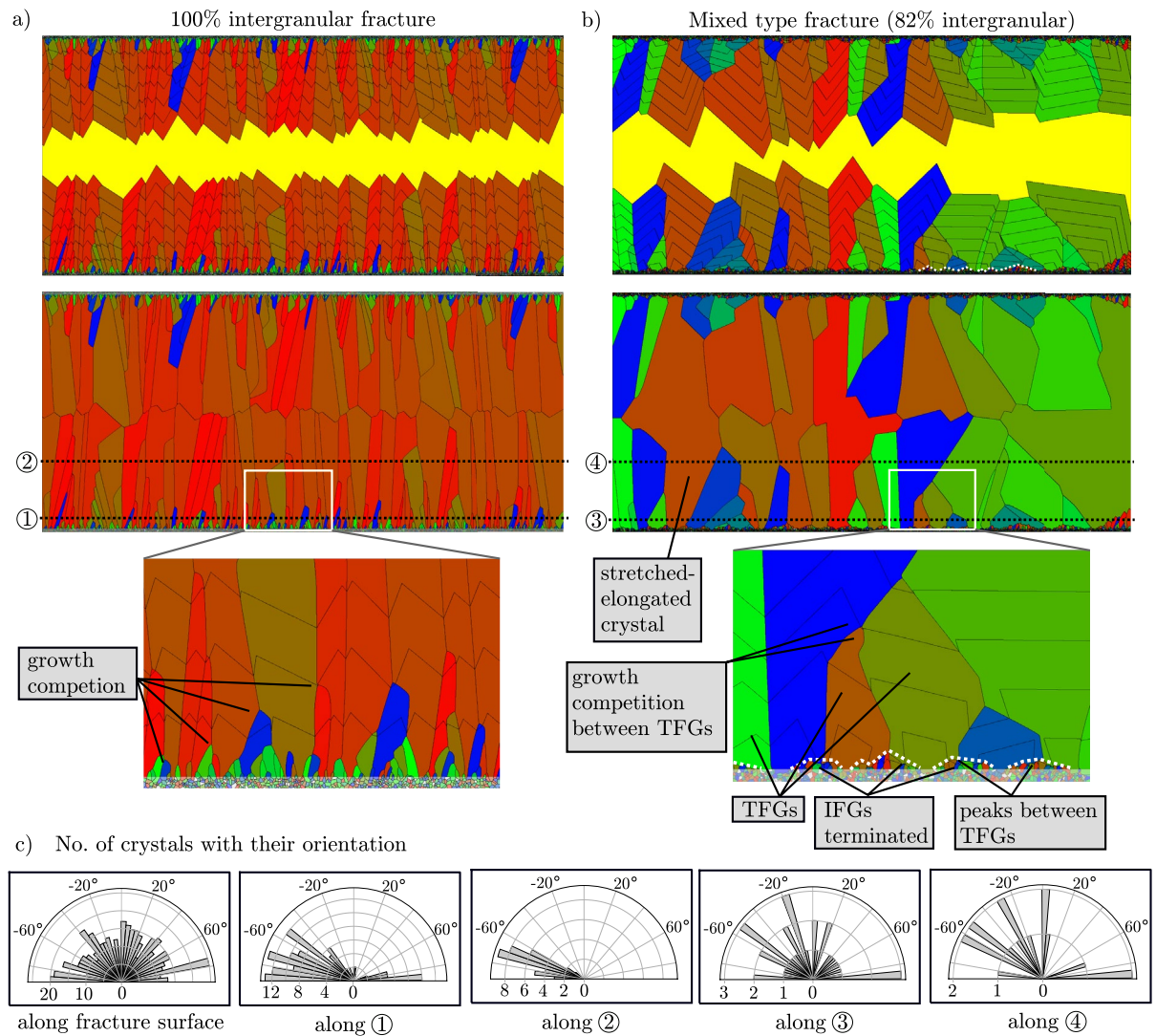


Figure 7. (a) Pure intergranular and (b) mixed intergranular and transgranular fracturing ($\xi = 5$) with an aperture of $300 D_m$ (setups with marked TFGs in Supporting Information S1). The images in the middle row depict the fully sealed vein, the images in the top row show intermediate crystal growth stages (marked by black lines) with liquid phase filling the pores (yellow). The bottom row shows an enlarged inset of the fully sealed vein close to the fracture wall (white box in middle row). (c) Rose diagram indicates the crystallographic orientation (c-axis) of the crystals with respect to the fracture opening vector along profile lines 1–4 and at the fracture surface in the host rock.

of the IFGs can grow into the open fracture, forming wedge-shaped groups of crystals, where the largest crystals occur in the middle between the two TFGs (white dotted line in Figure 7b). A few TFGs bridge with their opposite crystal fragment and form stretched-elongated crystals, while most crystals bridge with a differently oriented crystal like in the $30 D_m$ vein (median line is visible).

The grain orientation in the host rock and along profile lines 1–4 in the vein is depicted as a rose diagram in Figure 7c. In mixed-type fractures, due to their increased growth rate, TFGs expand laterally and survive even if they are unfavorably oriented, which also results in an inhomogeneous growth front. In contrast, when all grains fracture intergranularly, only favorably oriented crystals survive and terminate less favorably oriented crystals close to the rim (Figures 7a and 7c). Here, the lattice preferred orientation in the vein is much stronger (profile line 2). The surviving crystals form elongated-blocky and fibrous crystals and are narrower than in the vein with the mixed type fracturing. The growth front in veins on pure IFGs tends to stay more regular and homogeneous.

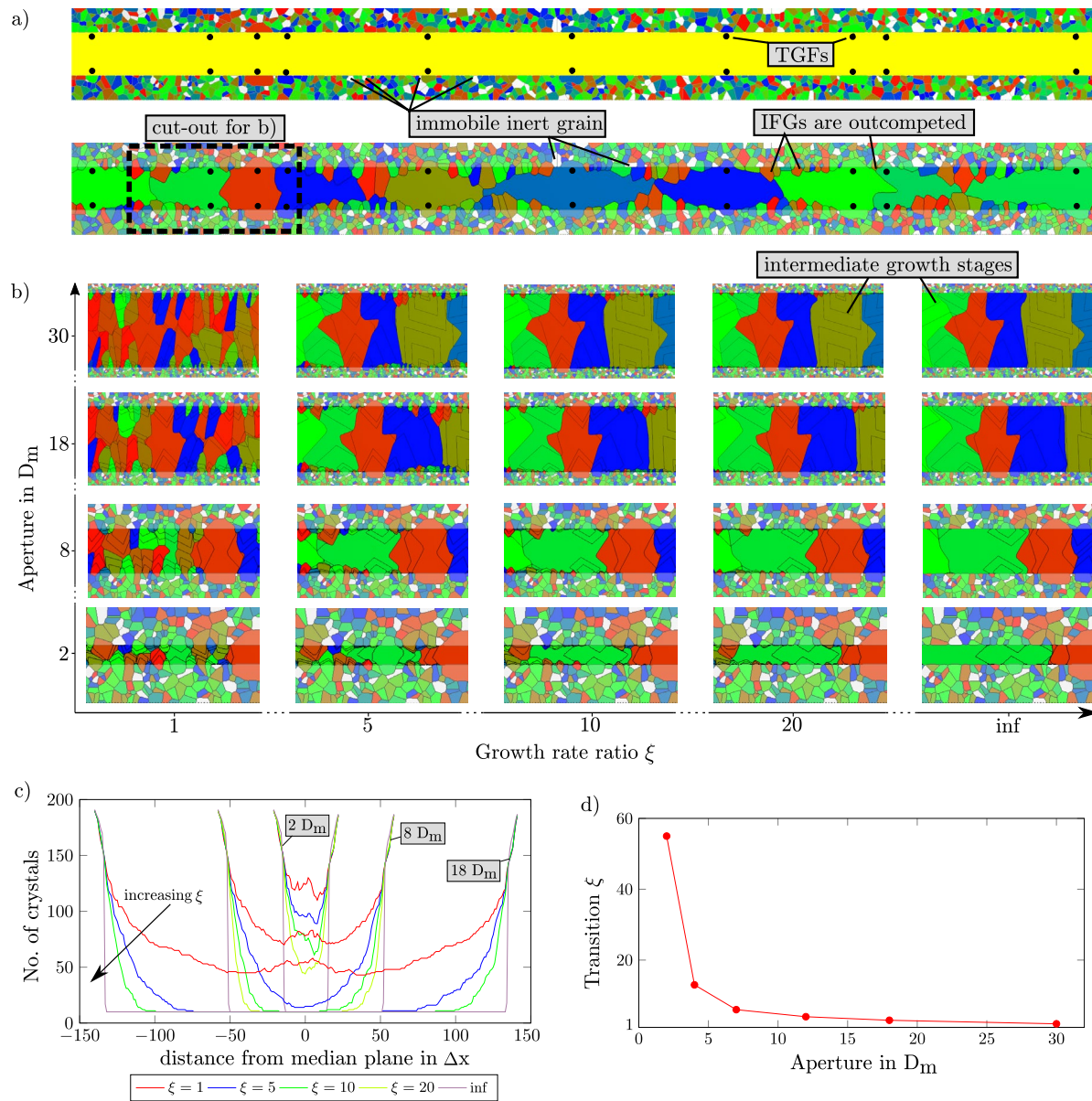


Figure 8. (a) Simulation setup and fully sealed vein ($8D_m$) ($\xi = 5$) with $\sim 82\%$ intergranularly broken grains on the fracture showing the effect of fracture-type controlled growth rate difference. The black dots indicate the location of the transgranularly fractured grains (TGFs), secondary minerals (e.g., quartz) are highlighted in light gray. Cut-out for (b) is marked with black dashed line. (b) Morphology diagram with different growth rate ratios ξ between intergranularly and transgranularly fractured grains. Black isolines indicate intermediate growth stages during sealing. (c) Number of crystals with respect to the distance from the median plane in the vein ($30D_m$ plot in Supporting Information S1). (d) Plot of transition ξ , which indicates when only TGFs touch in the vein center.

3.2. Effect of Growth Rate Ratio ξ Between TGFs and IFGs

In this section, we vary the relative growth rate of TGFs with respect to IFGs by assigning a coefficient $\xi = 1, 5, 10, 20, \text{inf.}$, where $\xi = 1$ implies no coating of IFGs. The term inf. indicates completely coated intergranular fractured calcite grains, which do not grow. The steps in between describe partly coated intergranular fractured calcite grains. We use a simulation setup with fracture apertures of 2, 8, 18, and $30D_m$. Figure 8a depicts the setup for an aperture of $8D_m$ ($220 \times 2500\Delta x$), where the black dots indicate the location of the TGFs. Additionally, we highlight accessory minerals (e.g., quartz grains) in the simulation setup in light gray in the forthcoming sections. Since the fluid in the open fracture is assumed to be supersaturated with respect to calcium carbonate and the vein crystals can only grow on calcite host rock grains, these accessory minerals are treated as inert (non growing) phases.

When crystals on IFGs and TFGs fracture segments grow at the same rate ($\xi = 1$) either: (1) the two separated fragments of an TFG reconnect and form stretched crystals or (2) different TFGs or IFGs touch in the vein center (Figure 8b). The first process depends on the crystallographic orientation of the grain, where stretched crystals form more likely, when a fast-growing axis is (nearly) parallel to opening vector of the fracture (see e.g., Lander & Laubach, 2015). In the chosen setup, the second case is more dominant and a distinct median line develops in most of the veins. The crystal morphologies in the veins with $\xi = 1$ resembles the microstructures of pure intergranular (100%) or pure transgranular (0%) fractured surface (Figures 6a and 7a).

When the growth rate ratio ξ is increased the TFGs outcompete more IFGs and expand laterally. The lateral width of the crystals that reach the central part of the vein shows a dependence on the vein aperture, especially in case of $\xi = 5$. The increase of ξ results in fewer and wider surviving crystals at the vein center, but reduces the effect of the vein aperture on the width of these crystals (see Figure 8c). In the veins, where IFGs are not allowed to grow ($\xi = \text{inf}$), the width of the surviving crystals is independent of the vein aperture and can be related directly to the TFGs segments on the initial fracture surface.

We determine a *transition* ξ that corresponds to the ξ value at which only crystals that grow on TFGs reach the central part of the vein. Figure 8d gives the value of the transition ξ for different vein apertures. Crystals that grow on IFGs segments can only bridge with IFGs from the opposite fracture wall where the applied ξ is smaller than the transition ξ . It is important to note that the transition ξ depends on the distribution and percentage of TFGs; the example shown was determined for the particular fracture surface, that was chosen for the model, consisting of 82% of IFGs segments. However we hypothesize that the decrease of the transition ξ for increasing apertures observed in this case is similar in fractures of different structure.

3.3. Effect of Grain Size Distribution in Host Rock

Calcite grains in limestones can range from only a few μm , as in mudstone, up to several mm as in crystalline limestone (Dunham, 1962; Flügel, 2013). In addition, many of the limestone types consist of a mix of fine and coarse grains, as in wackestone or packstone, where various proportions of mm-sized grains are embedded in a finer-grained matrix.

To test the effects of the host rock grain size on the vein microstructure, we compare two types of host rock. One case is set up with similarly sized grains, representative of crystalline limestone or mudstone structure in limestones and the other case, with differently sized grains representing a wackestone structure (Figure 9). The boundary conditions of these simulations follow those as in Figure 5a. To reduce the computational costs a smaller domain ($12450 \times 900\Delta x$) was cut out (Figure 9a), in which approx. 8% of the volume comprises coarse grains (total of 14,460 grains in domain). Furthermore, a setup with a single big grain was extracted from the structure for the simulation with small apertures to further reduce computational time.

For both host rock types we investigate two cases, 100% transgranular fracturing and mixed type fracturing where only coarse grains are fractured transgranularly. In the veins with 100% transgranular fracturing (Figure 9b) similar vein morphologies develop for both types of host rock as in Figure 5c, namely stretched crystals in small apertures and bitaxial crystals in larger apertures. As expected, because of the absence of other grain boundaries, the coarse grain (in center) survives in all of the tested apertures, while the crystal width does not change significantly.

In the veins with mixed type fracturing ($\xi = 5$) the crystal morphologies that develop show the same trend of an increased termination of IFGs with increasing aperture in both host rock types as in the previous sections (Figure 6). However, with larger apertures ($>8 D_m$) the crystal morphologies in the veins differ in the two host rock types with the same aperture (Figure 9c), since the distance between TFGs is larger for the different sized grained host rock.

3.4. Effect of Inert Second Phases

Most limestones are not monomineralic. They can contain up to 50% of accessory phases, such as clay, quartz grains, feldspar and organic material. As the setup for all simulations assumes that the fluid in the fractures is supersaturated with respect to calcium carbonate, the vein crystals grow exclusively on the host

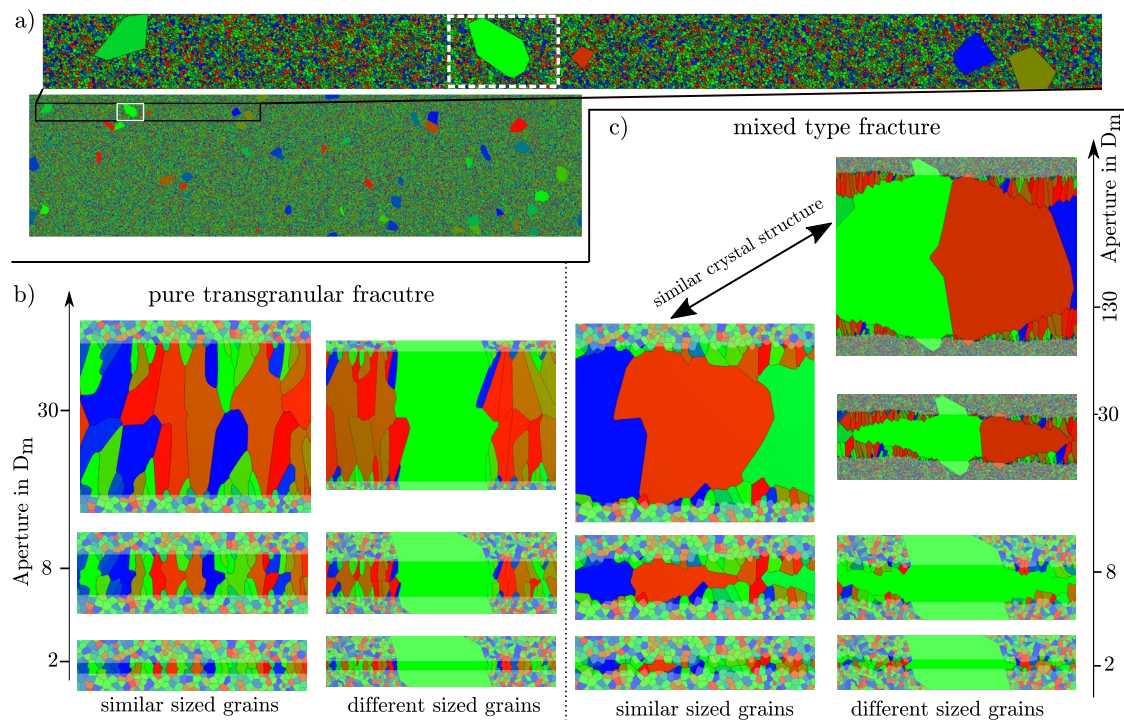


Figure 9. Unimodal versus bimodal grain size distribution in host rock. (a) Initial host rock. Extract indicates the simulated domain (black box and white dashed line). Comparison of same and different sized host rock with (b) 100% transgranularly fractured grains and (c) mixed type fracturing with intergranularly (small grains) and transgranularly (coarser grains) fractured grains ($\xi = 5$).

rock calcite grains that are exposed on the fracture surface. Therefore, we set all accessory minerals to be inert for crystal growth and mark them in the simulation results in light gray.

A morphology map with representative cut-outs from the fully sealed veins is depicted in Figures 10a and 10b for 82% and 100% intergranular fracturing respectively. For varying percentage of accessory minerals, we observe similar crystal morphologies as in the previous sections. However, in the small veins ($2 D_m$) the crystals become wider, whereas for larger apertures the crystal morphology in the vein interior is not significantly impacted by the amount of accessory minerals (Figures 10a–10c). Overall, the effect of inert/accessory minerals seems to be small for the tested cases, where they constitute up to 50% of the host rock grains.

3.5. Effect of Crystal Habit

Calcite in nature has a variety of crystal habits, which is controlled in a complex way by growth conditions, supersaturation and fluid chemistry. In order to determine how the microstructural evolution of calcite veins depends on the specific crystal habit, we investigate the crystal growth in rhombohedral and scalenohedral habits, which commonly occur in nature (Bishop et al., 1999; White & Culver, 2011). In addition, a variety of fracture apertures and fracture surface types are simulated with these crystal habits.

Figure 11a depicts representative cut-outs of rhombohedral and scalenohedral calcite morphologies on mixed type fractures (82% intergranular) using the same initial setup as for the simulations in Figure 8a. Overall, similar wide-blocky microstructures form for both crystal habits. The main differences are caused by the more elongated (fast-growing) c-axis for the scalenohedral habit. As a result, the unfavorably oriented crystals are less likely to bridge the vein at large apertures, even if they grow on TFGs (Figure 11a); $18 D_m$ and $30 D_m$). Thus, in the vein microstructure for the scalenohedral case, the size and shape of the bridging crystals is less homogeneous, compared to the rhombohedral cases. Here, slow-growing grains on IFGs bridge the veins only for the small fracture apertures (Figure 11a); $2 D_m$, $8 D_m$). However, in simu-

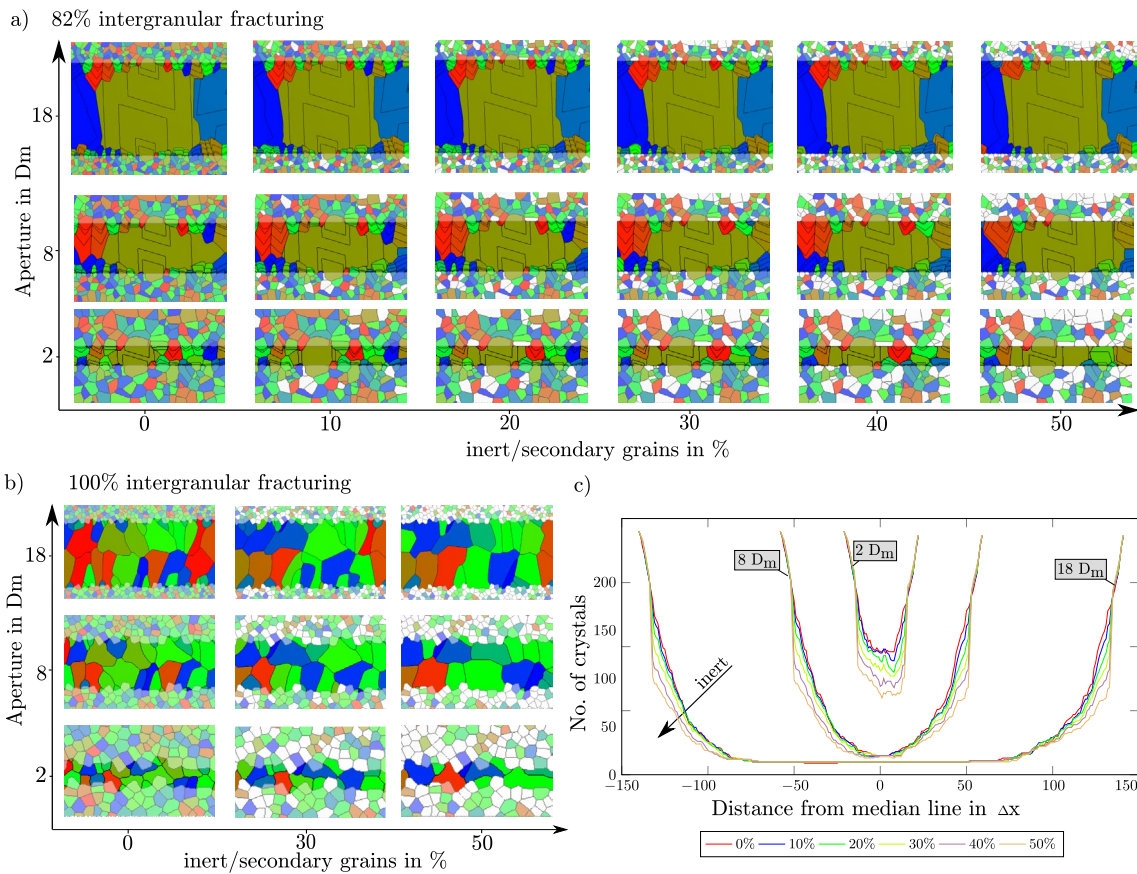


Figure 10. Proportion of accessory minerals: Morphology diagrams of vein microstructures with (a) 82% and (b) 100% intergranular fracturing. (c) Plot of the number of crystals with respect to the distance from the median plane in the vein apertures in (a).

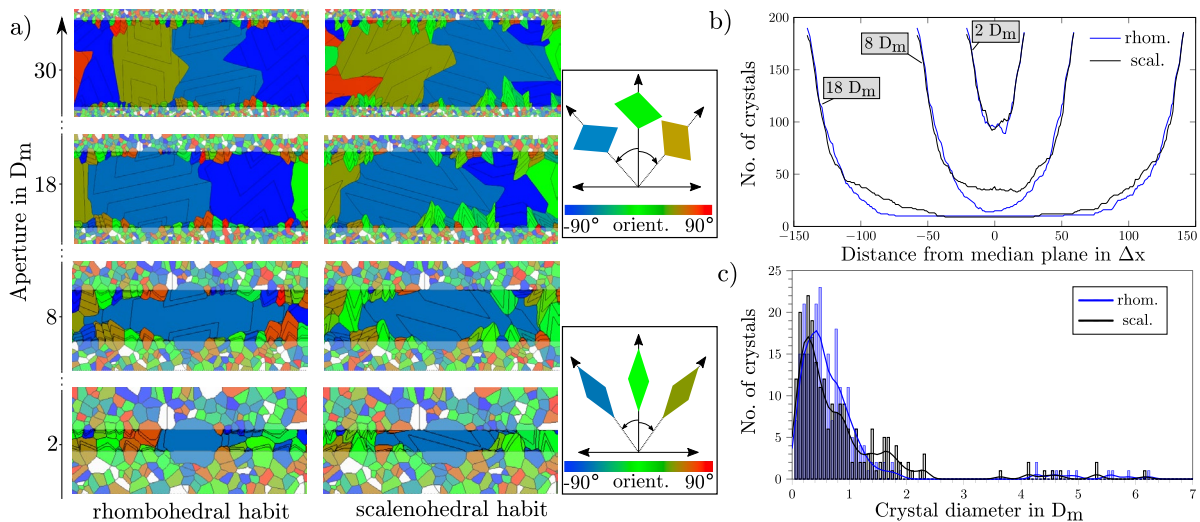


Figure 11. Scalenohedral vs rhombohedral calcite habit. (a) Vein morphology diagram, showing the effect of the initial fracture aperture. (b) Number of crystals with respect to the distance from the median plane in the vein for the apertures in (a). (c) Precipitated volume of each growing crystal for 8 D_m aperture for scalenohedral and rhombohedral calcite. For better visibility the diameter is computed from the precipitated volume of each precipitated crystal and scaled by the average host rock grain diameter D_m .

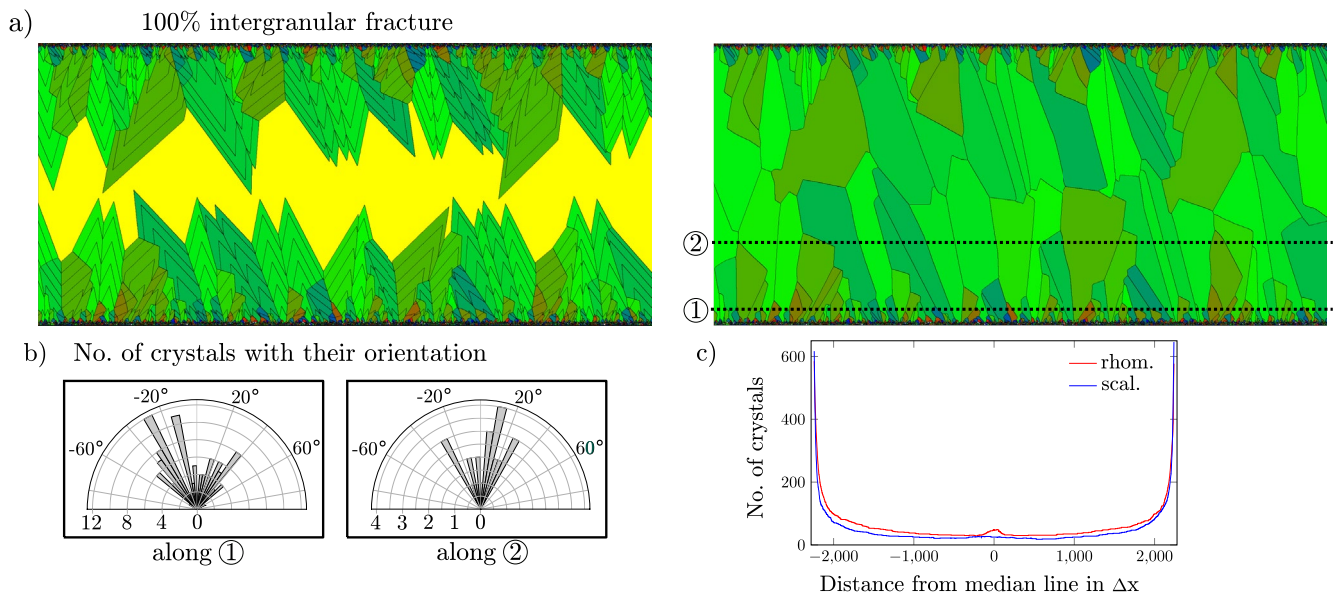


Figure 12. Aperture of $300D_m$ with scalenohedral crystal habit and 100% intergranular fracturing. (a) Intermediate stages (left) with timelines (in black) and fully sealed vein (right). (b) Rose diagrams indicate the crystallographic orientation of the crystals along the profile lines in (a). (c) Number of crystals with respect to the distance from the median plane in the vein.

lations with large apertures ($18D_m$, $30D_m$), favorably oriented crystals on IFGs reach larger sizes for the scalenohedral case (elongated c-axis). As shown in Figure 11b the number of crystals that reach the central part of the vein are similar in both cases for the larger apertures, whereas for the $8D_m$ case more crystals reach the median line with the scalenohedral habit. For the $8D_m$ aperture the precipitated volume of each crystal of both habits is depicted in Figure 11c, where an increased crystal size of the scalenohedral IFGs is observable.

Figures 7a and 12a show simulations of rhombohedral and scalenohedral calcite morphologies on 100% intergranular fracture surfaces for large apertures. In both cases the final vein microstructure consists of highly elongated crystals (with aspect ratio >10), that show crystallographically preferred orientation (Figures 7a and 7c-profile 2; Figure 12b) and a clear median line. In both cases the crystal size significantly increases toward the vein center, while the number of crystals decreases (Figure 12c), indicating crystallographically controlled growth competition, that is less pronounced on mixed type fracture surfaces (Figure 7b). Interestingly, for the scalenohedral habit the preferred orientation of the surviving large crystals is different compared to the simulations with rhombohedral habit (Figures 12b and 7c). This is attributed to the c/a ratio differences between the two habits used in the simulations. The final crystal structure looks similar for both habits, however the crystal shapes are blockier for the scalenohedral habit, whereas the crystals in the rhombohedral vein look more fibrous (Figures 7a and 12a). The growth front is less homogeneous, the median line is more serrated and the angles at triple grain-grain-liquid points during the grain growth are more acute in the scalenohedral case, compared to the simulations with the rhombohedral crystal habit.

3.6. Extension to 3D

An extension of the phase-field simulations from the 2D to 3D is straight forward, albeit increasing computational time. We perform an example simulation of a 3D vein in a host rock, which corresponds to a wackestone type in limestones. As in the 2D simulations (Figure 9), we assume, that the coarser host rock grains fracture transgranularly, whereas the finer-grained matrix fractures intergranularly. The fracture aperture is set to the size $32D_m$ similar to the 2D simulation in Figure 9c and the growth rate ratio ξ is set to 5. The generated domain (see Figure 13a) has the size of $2400 \times 700 \times 600\Delta x$ and comprises over 30,000 grains.

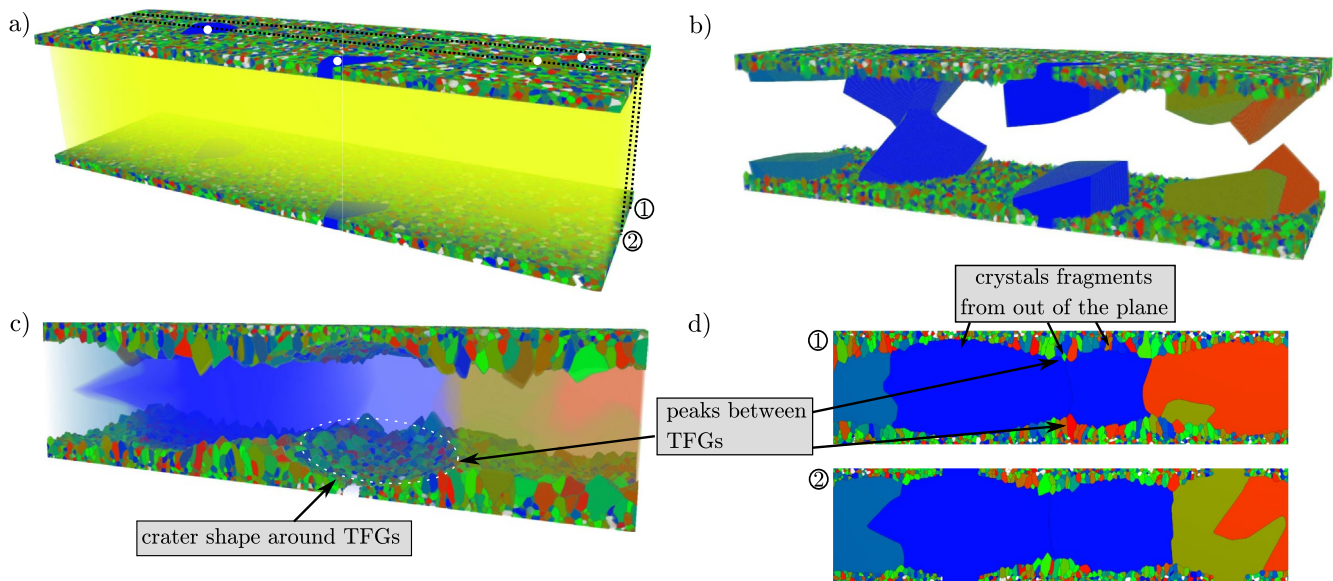


Figure 13. (a) 3D simulation setup of an open fracture in wackestone filled with liquid phase (yellow). White dots indicate coarse transgranularly fractured grains. (b) Bridging of crystals in intermediate stage. (c) Fully sealed fracture with transgranularly fractured grains (low opacity) filling the vein center. (d) 2D cut-outs along the profiles ① and ② in (a).

Similarly to the 2D experiments, crystals that grow on TFGs are the first to bridge the vein, joining up with their fragment that grows from the opposite side of the fracture; and then expanding laterally, while terminating the neighboring IFGs that grow at a slower rate (Figure 13b). The fully sealed vein in 3D is depicted in Figure 13c and along the cut-outs and in Figure 13d. All crystals that bridge the vein have originated on the TFGs (illustrated with low opacity in c), whereas crystals, growing on IFGs form a rim of small crystals along the vein margins, where grain size increases toward the boundary between two TFG grains, similar to the observations in the 2D simulations (Figure 9c). In contrast to the 2D models, in 3D the crystals can grow in all directions. This can be seen in the 2D cutouts of the 3D simulation (Figure 13d) as crystal "fragments" that are not connected to the host rock. Overall, however, this effect is small and does not significantly affect the microstructure of the vein.

4. Discussion

In this study, we systematically evaluated vein formation in a diverse range of limestones. Our numerical results show many similarities with natural vein microstructures and builds on the previous numerical works of Nollet et al. (2005); Lander and Laubach (2015); Prajapati et al. (2018); Spruzeniec et al. (2020, 2021), where controlling factors in vein formation are discussed.

Based on the results of our simulations, we identify five distinct crystal archetypes: stretched equidimensional, stretched elongated, wide-blocky, (bitaxial) blocky, (bitaxial) elongated blocky crystals. The results suggest that the most important factors which determine the vein microstructure are the type of fracturing (IFGs and TFGs, when $\xi > 1$) and the initial aperture of the fracture. In syntaxial veins stretched crystals form when transgranular fracturing occurs and the two parts of the same broken grain are sealed again by vein material, whereas bitaxial crystals grow either on intergranular fractures or misoriented transgranular fractures, where during the sealing process two unrelated crystals with different orientations join. The size of the initial fracture aperture determines if the vein is dominated by blocky or elongated crystals. Wide-blocky crystals form as stretched crystals that expand laterally due to the growth rate differences between intergranularly and transgranularly fractured grains (when $\xi > 1$). However, the formation of wide-blocky crystals is limited to special cases of mixed type fractures, where only 5%–20% grains have a faster growth rate than the rest (medium aperture Figure 6a). With an increased aperture, elongated blocky crystals form instead of wide-blocky crystals, since after the early

termination of IFGs, normal growth competition takes place between the fast-growing crystals on TFG surfaces (Figure 7b).

We focus on syntaxial vein formation in fractures, where the opening velocity of the fracture is higher than the velocity of crystal growth, so that crystals can obtain facets. This is a common scenario for vein formation in nature. Blocky crystal morphologies and growth competition structures, such as gradually increasing crystals sizes toward the vein interior due to the termination of unfavorably oriented crystals are considered to be a strong evidence for veins that form in open fractures (Bons et al., 2012). Our results, however, indicate that crystal growth in open fractures can also result in stretched crystal morphologies and absence of typical growth competition gradients in cases of transgranular and mixed type fracturing in small fracture apertures in equally sized and mixed-sized grain structures (Figures 5c, 6a, 8b and 8c).

When the fracture opening velocity is similar to the crystal growth velocity or multiple re-fracturing events happen the vein morphology is impacted by the opening velocity and trajectory (see e.g., Ankit, Selzer, et al., 2015; Ankit, Urai, & Nestler, 2015; Gale et al., 2010; Hilgers et al., 2001; Lander & Laubach, 2015; Prajapati et al., 2018; Urai et al., 1991). Those additional effects are not considered in this work, however in future studies further effects of opening trajectory and multiple (re)fracturing events can be investigated. This will help to better understand the formation of, for example, serrated grain boundaries.

Even though numerous laboratory studies show calcite growth rates on micro- and macroscale (e.g., Cao et al., 2018; Gratz et al., 1993; Lin & Singer, 2005; Nehrke et al., 2007) very few studies showcase crystal growth in open fractures (e.g., Lee & Morse, 1999) and how it compares to natural fracture opening velocities. Our studies could serve as a pathway for future laboratory experiments (analysis of natural rocks or growth experiments under hydrothermal reservoir conditions) in the direction of precipitation rates of specific facets with the focus on how rates change from rough to faceted growth and how nucleation discontinuities (clay coatings) affect the growth rates.

In the present work, we utilize the same vectors for surface energy (Equation 4) and kinetic anisotropy (Equation 7) and applied the same factor δ (in Equation 7) as in the previous studies of Spruženiece et al. (2020, 2021), which gives good agreement to microscopic observations. When a complete data set from crystal growth experiments for the growth velocities of the crystal facets and the growth velocity drop from rough to euhedral surfaces is available, both the anisotropy vectors and the factor δ (in Equation 7) can be calibrated (as in Prajapati, Abad Gonzalez, et al., 2020; Wendler et al., 2016 for quartz) and quantitative results about the cementation kinetics can be computed. Moreover, for a complete and precise comparison between natural and numerical veins additional data is required, for example: opening vector and shape of fracture surface, pressure, temperature, chemical composition of fluid.

The scaling of the fracture aperture in the simulations by the average host rock diameter D_m enables a direct comparison to natural veins, where the size of the host rock grains differ (e.g., crystalline limestone or mudstone) and helps understanding the conditions, under which the veins have formed. However, in bimodal host rocks, where grains have different sizes (e.g., wackestone, packstone) the scaling by D_m shows different crystal morphologies than in unimodal host rocks (see Figure 9c). For a better comparison of different bimodal host rocks and to unimodal host rocks, where the same mechanisms apply (e.g., fracturing type), the scaling should be extended in future works.

Very few studies (Lander & Laubach, 2015; Lander et al., 2008) have recognized that crystals within a vein can grow with different rates. Our modeling studies are based on prior observational works which inferred that differences in growth rates have to exist (Laubach et al., 2004). As shown by Spruženiece et al. (2020), these growth rate differences can be related to heterogeneities in fracture surface, where transgranularly broken grains grow faster than intergranularly broken grains due to the absence of coatings by secondary minerals which cover the growth surfaces. However, to obtain more quantitative predictions of the models the fracture surface should be investigated more detailed in future works. We simplify the system into fast and slow growing crystals and apply a different mobility for the two different grain classes (factor ξ), although in natural fractures multiple grow velocities for IFGs might be present depending on the amount and type of the coating. However, an adapted growth velocity distribution

only impacts the grain structure at the fracture rim and does not significantly influence the formation of wider TFGs.

At some point, when the coating is overgrown and crystal facets have formed, the growth velocities between IFGs and TFGs surfaces become similar. For the sake of simplicity, we prescribe a slower growth rate during the whole simulation, even though some IFGs might have formed facets. When this effect is incorporated (time varying ξ) similar microstructures form (e.g., wide-blocky veins) to those that form when a higher growth rate ratio ξ is prescribed in the early simulation stages, however the crystal morphologies at the rim slightly differ.

The vast majority of our studies were performed in 2D to limit computational costs. In 3D, a higher variation of the crystallographic orientation is possible and the growth of fast-growing crystals is less likely blocked by neighboring crystals as in 2D. However, the 3D simulation shows a similar microstructure as the corresponding 2D simulation (see Figures 9 and 13). This is in agreement with previous studies (Ankit, Selzer, et al., 2015; Ankit, Urai, & Nestler, 2015; Spruženiece et al., 2021; Wendler et al., 2016), which also obtained similar crystal morphologies in their 2D and 3D experiments. We expect that the other investigated parameters also show similar trends in 3D and the findings of our 2D studies can be transferred in 3D as well. Nonetheless, when a porosity and permeability analysis is requested (Kling et al., 2017; Prajapati, Abad Gonzalez, et al., 2020), 3D microstructures are indispensable.

Our results show that vein microstructures can be used as an evidence to infer the conditions of vein formation in nature. In Figure 14 different characteristic crystal morphologies in the simulated veins are compared to natural samples of calcite veins from Somerset coast in southern England and Oman mountains. These crystal morphologies in natural limestone are in accordance with the simulated veins and advocate the capability and accuracy of the phase-field method for modeling vein formation in limestones.

In contrast to the natural veins in mudstone (Figures 14a–14c and 14e) where a diverse crystal morphology exist due to different fracture types (inter-, transgranular, mixed type), the veins in crystalline limestone show mostly blocky crystals (Figures 14c and 2). This indicates that due to the larger grain size either the host rock grains preferentially fractures along weak grain boundaries or that a coating of the host rock grains has a smaller effect and only little fracture surface controlled growth competition occurs ($\xi \approx 1$).

5. Conclusion and Outlook

The presented simulations demonstrate the capability of the phase-field method to model crystal growth in veins, considering a large number of variables that are expected to influence vein formation in nature. We investigated the effects of fracture surface type, crystal habit, aperture, and grain size distribution in the host rock (analogue to mudstone, wackestone and crystalline limestone in natural limestones) on the vein formation, and created morphology diagrams to represent the results in a systematic way. The simulated vein microstructures show many similarities with natural veins in limestone and overall are in agreement with previous numerical studies (Lander & Laubach, 2015; Nolle et al., 2005; Prajapati et al., 2018).

Depending on the fracture type (intergranular, transgranular or mixed type) and the fracture aperture, different crystal morphologies are observed, such as equidimensional-stretched/ blocky (in small veins), elongated-blocky/ elongated-stretched, and wide blocky.

In future works the findings of this study can be extended into 3D as we showcased with an example. Although no pronounced microstructural differences were observed between 2D and 3D models, the 3D simulations can help to understand the porosity and permeability evolution in veins which is not possible when using the 2D models.

The vein sealing simulations can be combined in future works with mechanical fracture formation models (e.g., Prajapati, Herrmann, et al., 2020) to calculate the morphology of the cracks in porous and fully sealed veins with strong and weak grain boundaries. Furthermore, a coupling of the chemical driving force with

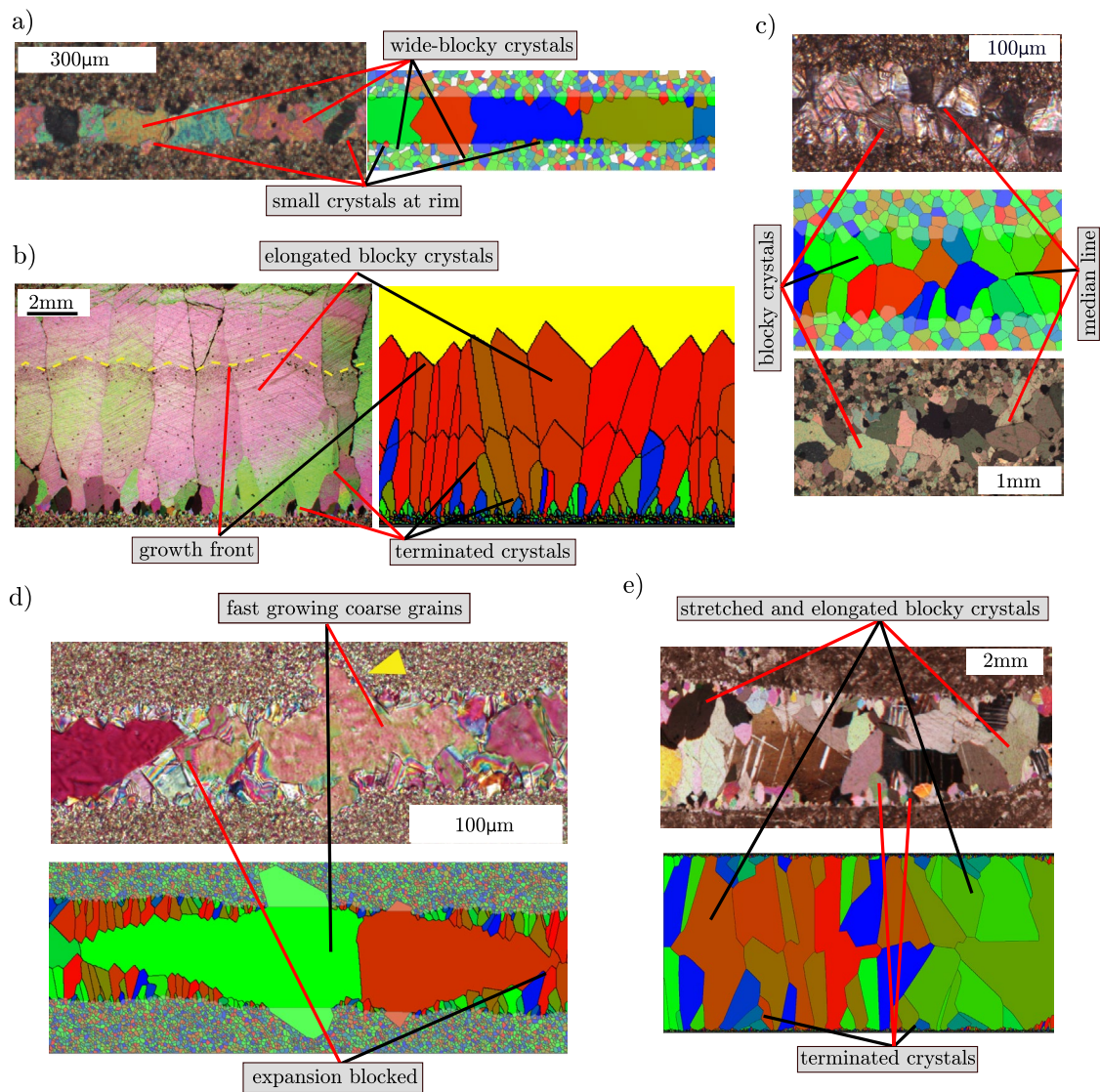


Figure 14. Comparison of simulated crystal morphologies with natural samples. The host rock types are: (a) mudstone from Lilstock beach (LB), UK; (b) mudstone from Oman mountains (OM); (c) bottom: crystalline limestone from OM; top: mudstone from Kilve beach, UK; (d) wackestone from OM; (e) mudstone from OM. The images (b, d, and e) are adapted from Arndt (2016) from Figure 2.43 (b), Figure 2.46D (d), 2.35B (e).

concentration equation and incorporating advective flow are possible to model different supersaturations and flow velocities.

Appendix A: Formation of Cross-Shaped Crystals

Here, we demonstrate the formation of cross-shaped crystals which are occasionally found in nature. The fully sealed vein from Section 3.2 with an aperture of $18 D_m$ and $\xi = 20$ is re-fractured with a high-angle to the first surface (Figure A1). Similarly, as in Section 3.2 the host rock grains are mostly fractured intergranularly, except two grains in the host rock and the big crystal in the re-fractured vein. Due to the high ξ the TFGs expand laterally while overgrowing and terminating the IFGs close to the rim, which results in a cross-shaped crystal.

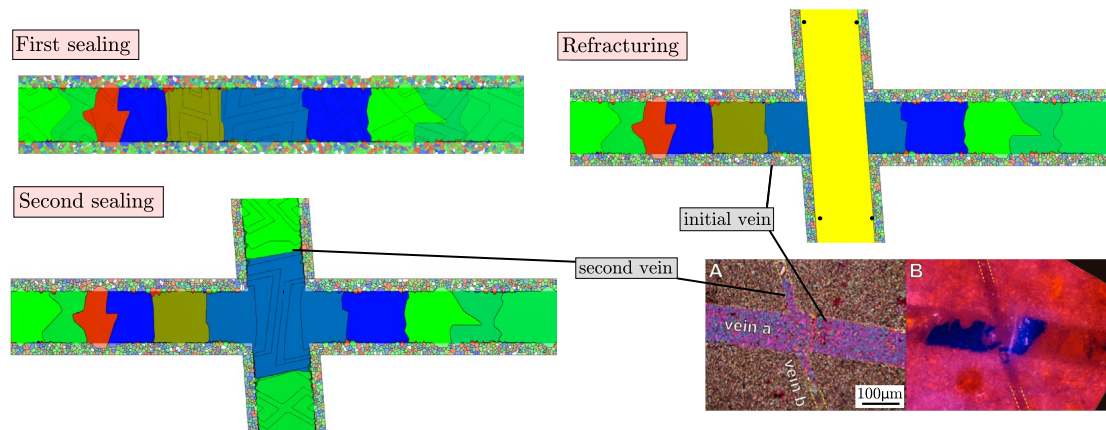


Figure A1. Evolution of cross-shaped crystal. Top left: Fully sealed vein after first fracturing. Black isolines show intermediate growth stages. Top right: Refractured vein with liquid phase (in yellow). Black dots show the location of TFGs in the host rock. Bottom left: Fully sealed vein after second fracturing. Bottom right: Micrograph with cross-shaped crystal from Oman Mountains: A: under cross-polarized light; B: CL image of A showing vein b formed later (adapted from Figure 3.14 in Arndt (2016)).

Data Availability Statement

The software package Pace3D version 2.5.1 was used for the generation of the simulation data sets. The software license can be purchased at Steinbeis Network (www.steinbeis.de) in the management of Britta Nestler and Michael Selzer under the subject area "Material Simulation and Process Optimization". The complete data set, on which this research article is based, can be accessed in the open-access repository at Späth et al. (2021) (<https://doi.org/10.5281/zenodo.4597529>).

Acknowledgments

The authors thank German Science Foundation DFG for funding this project, NE 822/34-1, UR 64/17-1. Support for the numerical solution has been contributed through the programs "RE: 35.14.01" and "MTET: 38.04.04" of the Helmholtz association. The authors thank Luuk L. Kleipool for help with Limestone nomenclature and for discussions about modelling different limestones. The authors acknowledge support by the state of Baden-Württemberg through bwHPC. The authors thank Julia Gale, John Hooker, and an anonymous reviewer for their constructive reviews. Open access funding enabled and organized by Projekt DEAL.

References

- Ajdkukiewicz, J. M., & Larese, R. E. (2012). How clay grain coats inhibit quartz cement and preserve porosity in deeply buried sandstones: Observations and experiments. *AAPG Bulletin*, 96(11), 2091–2119. <https://doi.org/10.1306/02211211075>
- Alexandrakis, C., Calò, M., Bouchaala, F., & Vavrycuk, V. (2014). Velocity structure and the role of fluids in the west bohemia seismic zone. *Solid Earth*, 5(2), 863. <https://doi.org/10.5194/se-5-863-2014>
- Almansour, A., Laubach, S. E., Bickel, J. E., & Schultz, R. A. (2020). Value-of-information analysis of a fracture prediction method. *SPE Reservoir Evaluation and Engineering*, 23(03), 811–823. <https://doi.org/10.2118/198906-pa>
- Ankit, K., Nestler, B., Selzer, M., & Reichardt, M. (2013). Phase-field study of grain boundary tracking behavior in crack-seal microstructures. *Contributions to Mineralogy and Petrology*, 166(6), 1709–1723. <https://doi.org/10.1007/s00410-013-0950-x>
- Ankit, K., Selzer, M., Hilgers, C., & Nestler, B. (2015). Phase-field modeling of fracture cementation processes in 3-d. *Journal of Geophysical Research: Solid Earth*, 4, 79. <https://doi.org/10.12783/jpsr.2015.0402.04>
- Ankit, K., Urai, J. L., & Nestler, B. (2015). Microstructural evolution in bitaxial crack-seal veins: A phase-field study. *Journal of Geophysical Research: Solid Earth*, 120, 3096–3118. <https://doi.org/10.1002/2015jb011934>
- Arndt, M. (2016). *On microstructures, fluid pathways and sealing of fractures in exhumed carbonate reservoir outcrop analogues in the Oman Mountains (Dissertation, RWTH Aachen, Aachen)*. Retrieved from <https://publications.rwth-aachen.de/record/567662>
- Arndt, M., Virgo, S., Cox, S. F., & Urai, J. L. (2014). Changes in fluid pathways in a calcite vein mesh (natih formation, Oman Mountains): Insights from stable isotopes. *Geofluids*, 14(4), 391–418. <https://doi.org/10.1111/gfl.12083>
- Aubert, I., Léonide, P., Lamarche, J., & Salardon, R. (2020). Diagenetic evolution of fault zones in urgonian microporous carbonates, impact on reservoir properties (provence-southeast France). *Solid Earth*, 11(4), 1163–1186. <https://doi.org/10.5194/se-11-1163-2020>
- Barber, D., & Wenk, H.-R. (1979). Deformation twinning in calcite, dolomite, and other rhombohedral carbonates. *Physics and Chemistry of Minerals*, 5(2), 141–165. <https://doi.org/10.1007/bf00307550>
- Becker, S., Hilgers, C., Kukla, P. A., & Urai, J. L. (2011). Crack-seal microstructure evolution in bi-mineralic quartz-chlorite veins in shales and siltstones from the rwth-1 well, Aachen, Germany. *Journal of Structural Geology*, 33(4), 676–689. <https://doi.org/10.1016/j.jsg.2011.01.001>
- Bishop, A., Woolley, A., & Hamilton, W. (1999). *Cambridge guide to minerals, rocks and fossils*. Cambridge University Press.
- Bons, P. D. (2001). Development of crystal morphology during uniaxial growth in a progressively widening vein: I. the numerical model. *Journal of Structural Geology*, 23(6–7), 865–872. [https://doi.org/10.1016/s0191-8141\(00\)00159-0](https://doi.org/10.1016/s0191-8141(00)00159-0)
- Bons, P. D., Elburg, M. A., & Gomez-Rivas, E. (2012). A review of the formation of tectonic veins and their microstructures. *Journal of Structural Geology*, 43, 33–62. <https://doi.org/10.1016/j.jsg.2012.07.005>
- Boullier, A.-M., & Robert, F. (1992). Palaeoseismic events recorded in Archaean gold-quartz vein networks, val d'or, abitibi, quebec, canada. *Journal of Structural Geology*, 14(2), 161–179. [https://doi.org/10.1016/0191-8141\(92\)90054-z](https://doi.org/10.1016/0191-8141(92)90054-z)
- Cao, B., Stack, A. G., Steefel, C. I., DePaolo, D. J., Lammers, L. N., & Hu, Y. (2018). Investigating calcite growth rates using a quartz crystal microbalance with dissipation (qcm-d). *Geochimica et Cosmochimica Acta*, 222, 269–283. <https://doi.org/10.1016/j.gca.2017.10.020>

- Cobbold, P. R., Zanella, A., Rodrigues, N., & Løseth, H. (2013). Bedding-parallel fibrous veins (beef and cone-in-cone): Worldwide occurrence and possible significance in terms of fluid overpressure, hydrocarbon generation and mineralization. *Marine and Petroleum Geology*, 43, 1–20. <https://doi.org/10.1016/j.marpetgeo.2013.01.010>
- Cox, S. F. (2007). Structural and isotopic constraints on fluid flow regimes and fluid pathways during upper crustal deformation: An example from the taemas area of the lachlan orogen, se australia. *Journal of Geophysical Research*, 112. <https://doi.org/10.1029/2006jb004734>
- Cox, S. F., Etheridge, M., & Wall, V. (1987). The role of fluids in syntectonic mass transport, and the localization of metamorphic vein-type ore deposit. *Ore Geology Reviews*, 2(1–3), 65–86. [https://doi.org/10.1016/0169-1368\(87\)90024-2](https://doi.org/10.1016/0169-1368(87)90024-2)
- Dunham, R. J. (1962). *Classification of carbonate rocks according to depositional textures*.
- Durney, D. (1973). Incremental strains measured by syntectonic crystal growths. *Gravity and tectonics*, 67–96.
- Fisher, D. M., & Brantley, S. L. (1992). Models of quartz overgrowth and vein formation: Deformation and episodic fluid flow in an ancient subduction zone. *Journal of Geophysical Research*, 97(B13), 20043–20061. <https://doi.org/10.1029/92jb01582>
- Fix, G. J. (1982). *Phase field methods for free boundary problems*.
- Flügel, E. (2013). *Microfacies of carbonate rocks: Analysis, interpretation and application*. Springer Science & Business Media.
- Gale, J. F. W., Lander, R. H., Reed, R. M., & Laubach, S. E. (2010). Modeling fracture porosity evolution in dolostone. *Journal of Structural Geology*, 32(9), 1201–1211. <https://doi.org/10.1016/j.jsg.2009.04.018>
- Goldschmidt, V. (1913). *Atlas der kristallformen* (Vol. 2). C. Winter.
- Gratz, A., Hillner, P., & Hansma, P. (1993). Step dynamics and spiral growth on calcite. *Geochimica et Cosmochimica Acta*, 57(2), 491–495. [https://doi.org/10.1016/0016-7037\(93\)90449-7](https://doi.org/10.1016/0016-7037(93)90449-7)
- Gunasekaran, S., Anbalagan, G., & Pandi, S. (2006). Raman and infrared spectra of carbonates of calcite structure. *Journal of Raman Spectroscopy*, 37(9), 892–899. <https://doi.org/10.1002/jrs.1518>
- Gutjahr, A., Dabringhaus, H., & Lacmann, R. (1996). Studies of the growth and dissolution kinetics of the caco3 polymorphs calcite and aragonite ii. The influence of divalent cation additives on the growth and dissolution rates. *Journal of Crystal Growth*, 158(3), 310–315. [https://doi.org/10.1016/0022-0248\(95\)00447-5](https://doi.org/10.1016/0022-0248(95)00447-5)
- Hartman, P., & Perdok, W. (1955a). On the relations between structure and morphology of crystals. I. *Acta Crystallographica*, 8(1), 49–52. <https://doi.org/10.1107/s0365110x55000121>
- Hartman, P., & Perdok, W. (1955b). On the relations between structure and morphology of crystals. II. *Acta Crystallographica*, 8(9), 521–524. <https://doi.org/10.1107/s0365110x55001679>
- Hartman, P., & Perdok, W. (1955c). On the relations between structure and morphology of crystals. III. *Acta Crystallographica*, 8(9), 525–529. <https://doi.org/10.1107/s0365110x55001680>
- Hilgers, C., Koehn, D., Bons, P., & Urai, J. (2001). Development of crystal morphology during uniaxial growth in a progressively widening vein: II. Numerical simulations of the evolution of antitaxial fibrous veins. *Journal of Structural Geology*, 23(6–7), 873–885. [https://doi.org/10.1016/s0191-8141\(00\)00160-7](https://doi.org/10.1016/s0191-8141(00)00160-7)
- Hilgers, C., & Urai, J. L. (2002). Microstructural observations on natural syntectonic fibrous veins: Implications for the growth process. *Tectonophysics*, 352(3–4), 257–274. [https://doi.org/10.1016/s0040-1951\(02\)00185-3](https://doi.org/10.1016/s0040-1951(02)00185-3)
- Hötzer, J., Reiter, A., Hierl, H., Steinmetz, P., Selzer, M., & Nestler, B. (2018). The parallel multi-physics phase-field framework pace3d. *Journal of computational science*, 26, 1–12. <https://doi.org/10.1016/j.jocs.2018.02.011>
- Hubert, J., Emmerich, H., & Urai, J. (2009). Modelling the evolution of vein microstructure with phase-field techniques—a first look. *Journal of Metamorphic Geology*, 27(7), 523–530. <https://doi.org/10.1111/j.1525-1314.2009.00839.x>
- Kling, T., Schwarz, J.-O., Wendler, F., Enzmann, F., & Blum, P. (2017). Fracture flow due to hydrothermally induced quartz growth. *Advances in Water Resources*, 107, 93–107. <https://doi.org/10.1016/j.advwatres.2017.06.011>
- Lander, R. H., Larese, R. E., & Bonnell, L. M. (2008). Toward more accurate quartz cement models: The importance of euhedral versus noneuhedral growth rates. *AAPG Bulletin*, 92(11), 1537–1563. <https://doi.org/10.1306/07160808037>
- Lander, R. H., & Laubach, S. E. (2015). Insights into rates of fracture growth and sealing from a model for quartz cementation in fractured sandstones. *GSA Bulletin*, 127(3–4), 516–538. <https://doi.org/10.1130/b31092.1>
- Langer, J. S. (1980). Instabilities and pattern formation in crystal growth. *Reviews of Modern Physics*, 52(1), 1. <https://doi.org/10.1103/revmodphys.52.1>
- Langer, J. S. (1986). Models of pattern formation in first-order phase transitions. In *Directions in condensed matter physics: Memorial volume in honor of shang-keng ma* (pp. 165–186). World Scientific. https://doi.org/10.1142/9789814415309_0005
- Laubach, S. E., Lander, R. H., Criscenti, L. J., Anovitz, L. M., Urai, J. L., Pollyea, R., et al. (2019). The role of chemistry in fracture pattern development and opportunities to advance interpretations of geological materials. *Reviews of Geophysics*, 57(3), 1065–1111. <https://doi.org/10.1029/2019rg000671>
- Laubach, S. E., Reed, R. M., Olson, J. E., Lander, R. H., & Bonnell, L. M. (2004). Coevolution of crack-seal texture and fracture porosity in sedimentary rocks: Cathodoluminescence observations of regional fractures. *Journal of Structural Geology*, 26(5), 967–982. <https://doi.org/10.1016/j.jsg.2003.08.019>
- Lee, Y.-J., & Morse, J. W. (1999). Calcite precipitation in synthetic veins: Implications for the time and fluid volume necessary for vein filling. *Chemical Geology*, 156(1–4), 151–170. [https://doi.org/10.1016/s0009-2541\(98\)00183-1](https://doi.org/10.1016/s0009-2541(98)00183-1)
- Leitner, C., Friedl, G., Baumann, S., & Bieniok, A. (2014). Excavation and humidity induced extension veins of mudrock clasts in a ductile rock salt matrix, filled with secondary halite deposits (northern calcareous Alps, Austria, Bavaria). *Zeitschrift der Deutschen Gesellschaft für Geowissenschaften*, 165, 77–90. <https://doi.org/10.1127/1860-1804/2014/0061>
- Lin, Y.-P., & Singer, P. C. (2005). Effects of seed material and solution composition on calcite precipitation. *Geochimica et Cosmochimica Acta*, 69(18), 4495–4504. <https://doi.org/10.1016/j.gca.2005.06.002>
- McNamara, D. D., Lister, A., & Prior, D. J. (2016). Calcite sealing in a fractured geothermal reservoir: Insights from combined ebsd and chemistry mapping. *Journal of Volcanology and Geothermal Research*, 323, 38–52. <https://doi.org/10.1016/j.jvolgeores.2016.04.042>
- Meng, Q., Hooker, J. N., & Cartwright, J. (2019). Progressive accretion of antitaxial crystal fibres: Implications for the kinematics and dynamics of vein dilation. *Journal of Structural Geology*, 126, 25–36. <https://doi.org/10.1016/j.jsg.2019.05.006>
- Nehrknecht, G., Reichart, G.-J., Van Cappellen, P., Meile, C., & Bijma, J. (2007). Dependence of calcite growth rate and sr partitioning on solution stoichiometry: Non-kossel crystal growth. *Geochimica et Cosmochimica Acta*, 71(9), 2240–2249. <https://doi.org/10.1016/j.gca.2007.02.002>
- Nestler, B., Garcke, H., & Stinner, B. (2005). Multicomponent alloy solidification: Phase-field modeling and simulations. *Physical Review E*, 71(4), 041609. <https://doi.org/10.1103/physreve.71.041609>
- Nollet, S., Urai, J. L., Bons, P. D., & Hilgers, C. (2005). Numerical simulations of polycrystal growth in veins. *Journal of Structural Geology*, 27(2), 217–230. <https://doi.org/10.1016/j.jsg.2004.10.003>

- Okamoto, A., Saishu, H., Hirano, N., & Tsuchiya, N. (2010). Mineralogical and textural variation of silica minerals in hydrothermal flow-through experiments: Implications for quartz vein formation. *Geochimica et Cosmochimica Acta*, 74(13), 3692–3706. <https://doi.org/10.1016/j.gca.2010.03.031>
- Paquette, J., & Reeder, R. J. (1990). New type of compositional zoning in calcite: Insights into crystal-growth mechanisms. *Geology*, 18(12), 1244–1247. [https://doi.org/10.1130/0091-7613\(1990\)018<1244:ntoczi>2.3.co;2](https://doi.org/10.1130/0091-7613(1990)018<1244:ntoczi>2.3.co;2)
- Passchier, C. W., & Trouw, R. A. (2005). *Microtectonics*. Springer Science & Business Media.
- Philipp, S. L. (2008). Geometry and formation of gypsum veins in mudstones at watchet, somerset, sw England. *Geological Magazine*, 145(6), 831–844. <https://doi.org/10.1017/s0016756808005451>
- Plummer, L. N., Parkhurst, D. L., & Wigley, T. M. L. (1979). Critical review of the kinetics of calcite dissolution and precipitation. In *Chemical modeling in aqueous systems* (pp. 537–573). <https://doi.org/10.1021/bk-1979-0093.ch025>
- Prajapati, N., Abad Gonzalez, A., Selzer, M., Nestler, B., Busch, B., & Hilgers, C. (2020). Quartz cementation in polycrystalline sandstone: Insights from phase-field simulations. *Journal of Geophysical Research*, 125, e2019JB019137. <https://doi.org/10.1029/2019jb019137>
- Prajapati, N., Herrmann, C., Späth, M., Schneider, D., Selzer, M., & Nestler, B. (2020). Brittle anisotropic fracture propagation in quartz sandstone: Insights from phase-field simulations. *Computational Geosciences*, 1–16. <https://doi.org/10.1007/s10596-020-09956-3>
- Prajapati, N., Selzer, M., & Nestler, B. (2017). Computational modeling of calcite cementation in saline limestone aquifers: A phase-field study. *Geothermal Energy*, 5(1), 15. <https://doi.org/10.1186/s40517-017-0072-1>
- Prajapati, N., Selzer, M., Nestler, B., Busch, B., & Hilgers, C. (2018). Modeling fracture cementation processes in calcite limestone: A phase-field study. *Geothermal Energy*, 6(1), 7. <https://doi.org/10.1186/s40517-018-0093-4>
- Ramsay, J. G., & Huber, M. I. (1983). *The techniques of modern structural geology: Strain analyses* (Vol. 1). Course Technology.
- Schmidegg, O. (1928). Über geregelte wachstumsgefüge. *Jb. Geol. Bundesanstalt (Austria)*, 78, 1–52.
- Sekkal, W., & Zaoui, A. (2013). Nanoscale analysis of the morphology and surface stability of calcium carbonate polymorphs. *Scientific Reports*, 3(1), 1–10. <https://doi.org/10.1038/srep01587>
- Sibson, R. H., Robert, F., & Poulsen, K. H. (1988). High-angle reverse faults, fluid-pressure cycling, and mesothermal gold-quartz deposits. *Geology*, 16(6), 551–555. [https://doi.org/10.1130/0091-7613\(1988\)016<0551:HARFFP>2.3.CO;2](https://doi.org/10.1130/0091-7613(1988)016<0551:HARFFP>2.3.CO;2)
- Späth, M., Spruženiece, L., Urai, J. L., Selzer, M., Arndt, M., & Nestler, B. (2021). *Data set for phase-field studies of crystal growth in single-seal syntaxial veins in limestone [data set]*. Zenodo. <https://doi.org/10.5281/zenodo.4597529>
- Spruženiece, L., Späth, M., Urai, J. L., Ukar, E., Selzer, M., & Nestler, B. (2021). Wide-blocky veins explained by dependency of crystal growth rate on fracture surface type: Insights from phase-field modeling. *Geology*, 49(6), 641–646. <https://doi.org/10.1130/G48472.1>
- Spruženiece, L., Späth, M., Urai, J. L., Ukar, E., Selzer, M., Nestler, B., & Schwedt, A. (2020). Formation of wide-blocky calcite veins by extreme growth competition. *Journal of the Geological Society*. <https://doi.org/10.1144/jgs2020-104>
- Steinbach, I. (2009). Phase-field models in materials science. *Modelling and Simulation in Materials Science and Engineering*, 17(7), 073001. <https://doi.org/10.1088/0965-0393/17/7/073001>
- Urai, J. L., Williams, P., & Van Roermund, H. (1991). Kinematics of crystal growth in syntectonic fibrous veins. *Journal of Structural Geology*, 13(7), 823–836. [https://doi.org/10.1016/0191-8141\(91\)90007-6](https://doi.org/10.1016/0191-8141(91)90007-6)
- Wendler, F., Okamoto, A., & Blum, P. (2016). Phase-field modeling of epitaxial growth of polycrystalline quartz veins in hydrothermal experiments. *Geofluids*, 16(2), 211–230. <https://doi.org/10.1111/gfl.12144>
- White, W. B., & Culver, D. C. (2011). (p. 500). Encyclopedia of caves. In Academic Press.
- Williams, R. T., Farver, J. R., Onasch, C. M., & Winslow, D. F. (2015). An experimental investigation of the role of microfracture surfaces in controlling quartz precipitation rate: Applications to fault zone diagenesis. *Journal of Structural Geology*, 74, 24–30. <https://doi.org/10.1016/j.jsg.2015.02.011>
- Zhang, J., & Adams, J. B. (2002). Facet: A novel model of simulation and visualization of polycrystalline thin film growth. *Modelling and Simulation in Materials Science and Engineering*, 10(4), 381. <https://doi.org/10.1088/0965-0393/10/4/302>